

Ministry of Science and Higher Education of the Russian Federation
ITMO University

GRADUATION THESIS

**SECOND-ORDER NONLINEAR PROCESSES IN ALL-DIELECTRIC AND
HYBRID METAL-DIELECTRIC NANOSTRUCTURES**

Author Anna A. Nikolaeva
(full name)

Subject area 16.04.01 Technical Physics
(code, name of program track)

Degree level Master
(Bachelor, Master, Engineer)*

Thesis supervisor Mihail I. Petrov, PhD
(surname, initials, academic title, degree)

St. Petersburg, 2020

Student Anna A. Nikolaeva

Group Z42401 Faculty/Institute/Cluster PhE

Subject area, program/major 16.04.01 Technical Physics

Nanophotonics and metamaterials

Date of defense “19” June 2020

Secretary of State Exam Commission Anna Yu. Shiker

Министерство науки и высшего образования Российской Федерации
ФЕДЕРАЛЬНОЕ ГОСУДАРСТВЕННОЕ АВТОНОМНОЕ ОБРАЗОВАТЕЛЬНОЕ УЧРЕЖДЕНИЕ ВЫСШЕГО ОБРАЗОВАНИЯ
“Национальный исследовательский университет ИТМО”

ВЫПУСКНАЯ КВАЛИФИКАЦИОННАЯ РАБОТА

**НЕЛИНЕЙНЫЕ ПРОЦЕССЫ ВТОРОГО ПОРЯДКА В
ДИЭЛЕКТРИЧЕСКИХ И ГИБРИДНЫХ МЕТАЛ-ДИЭЛЕКТРИЧЕСКИХ
НАНОСТРУКТУРАХ**

Автор Николаева Анна Андреевна
(Фамилия, Имя, Отчество)

Направление подготовки (специальность) 16.04.01 Техническая физика
(код, наименование)

Квалификация магистр
(бакалавр, магистр)*

Руководитель ВКР Петров М.И., к.ф.-м.н.
(Фамилия, И., О., ученое звание, степень)

Санкт-Петербург, 2020 г.

Обучающийся Николаева Анна Андреевна
Группа Z42401 Факультет/институт/кластер Физико-технический факультет
Направленность (профиль), специализация 16.04.01 Техническая физика
Нанопотоника и метаматериалы

Дата защиты “19” июня 2020г.

Секретарь ГЭК Шикер Анна Юрьевна
(ФИО)

Ministry of Science and Higher Education of the Russian Federation
ITMO University

APPROVED

Head of educational program

Andrey A. Bogdanov _____
(signature)

« 10 » « December » 2019

OBJECTIVES
FOR A GRADUATION THESIS

Student Anna A. Nikolaeva

Group Z42401 **Faculty/Institute/Cluster** PhE

Degree level Master

Subject area 16.04.01 Technical Physics

Major Nanophotonics and metamaterials

Specialization Theoretical methods and approaches of nanophotonics and metamaterials

1 Thesis topic Second-order nonlinear processes in all-dielectric and hybrid metal-dielectric nanostructures

Thesis supervisor Mihail I. Petrov, ITMO University, Research fellow, PhD

2 Deadline for submission of complete thesis « 01 » « June » 2020

3 Requirements and premise for the thesis

Study the spontaneous parametric down-conversion of light by resonant spherical dielectric nanoparticle and second harmonic generation by bi-resonant hybrid metal-dielectric nanoantenna.

4 Content of the thesis (list of key issues)

Introduction

1 Methods

2 Spontaneous parametric down-conversion by dielectric nanoparticle

2.1 Linear Kerker effect

2.2 Non-linear generation of entangled photons

2.3 Directional emission from GaAs nanoparticle

2.4 Polarization correlations

3 Second harmonic generation by hybrid metal - dielectric nanoantenna

3.1 Analysis of the resonance properties of a hybrid nanoantenna

3.2 Second harmonic generation efficiency of a hybrid bi-resonance nanoantenna

Conclusion

5 List of graphic materials (with a list of required material)

This work includes 26 graphs

6 Source materials and publications

1. “Generation of Photon-Plasmon Quantum States in Nonlinear Hyperbolic Metamaterials”/ Poddubny A.N., Iorsh I.V., Sukhorukkov A.A. //Physical Review Letters. — 2016. — Vol. 117, no. 12. — Pp. 1–6.

2. “Second-harmonic generation in Mie-resonant dielectric nanoparticles made of noncentrosymmetric materials” / Kristina Frizyuk, Irina Volkovskaya, Daria Smirnova et al. //Physical Review B. — 2019. —Vol. 99, no. 7. — Pp. 1–18

3. “Reshaping the Second-Order Polar Response of Hybrid Metal–Dielectric Nanodimers” / Claude Renaut, Lukas Lang, Kristina Frizyuk et al. //Nano Letters. — 2019. — Vol. 19, no. 2. — Pp. 877–884

4. “Absorption and Scattering of Light by Small Particles” / C. Bohren, D. R. Huffman //Wiley Science Paperback Series, 1998.

5. “Spontaneous photon-pair generation from a dielectric nanoantenna” / Giuseppe Marino, Alexander S. Solntsev, Lei Xu et al. //Optica. —2019. — Nov. — Vol. 6, no. 11. — Pp. 1416–1422

7 Objectives issued on « 10 » « December » 2019

Thesis supervisor Mihail I.Petrov

Министерство науки и высшего образования Российской Федерации
ФЕДЕРАЛЬНОЕ ГОСУДАРСТВЕННОЕ АВТОНОМНОЕ ОБРАЗОВАТЕЛЬНОЕ УЧРЕЖДЕНИЕ ВЫСШЕГО ОБРАЗОВАНИЯ
"НАЦИОНАЛЬНЫЙ ИССЛЕДОВАТЕЛЬСКИЙ УНИВЕРСИТЕТ ИТМО"

УТВЕРЖДАЮ

Руководитель ОП

Богданов А.А. _____
(подпись)

« 10 » « декабря » 2019 г.

З А Д А Н И Е
НА ВЫПУСКНУЮ КВАЛИФИКАЦИОННУЮ РАБОТУ

Обучающийся Николаева Анна Андреевна

Группа Z42401 Факультет/институт/кластер Физико-технический факультет

Квалификация Магистр

Направление подготовки 16.04.01 Техническая физика

Направленность (профиль) образовательной программы

Нанопотоника и метаматериалы

Специализация Теоретические методы и подходы нанопотоники и метаматериалов

1 Тема ВКР Нелинейные процессы второго порядка в диэлектрических и гибридных металл-диэлектрических наноструктурах

Руководитель Петров Михаил Игоревич, Университет ИТМО, старший научный сотрудник, к.ф.-м.н.

2 Срок сдачи студентом законченной работы до « 01 » « июня » 2020 г.

3 Техническое задание и исходные данные к работе

Исследование спонтанного параметрического рассеяния света резонансной диэлектрической сферической наночастицей и генерации второй гармоники би-резонансной гибридной металл-диэлектрической наноантенной

4 Содержание выпускной квалификационной работы (перечень подлежащих разработке вопросов)

Введение

1 Методы

2 Спонтанное параметрическое рассеяние света диэлектрической наночастицей

2.1 Линейный эффект Керкера

2.2 Нелинейная генерация запутанных фотонов

2.3 Направленное испускание фотонов наночастицей из арсенида галлия

2.4 Поляризационные корреляции

3 Генерация второй гармоники от гибридной метал-диэлектрической наноантенны

3.1 Анализ резонансных свойств гибридной наноантенны

3.2 Эффективность генерации второй гармоники от гибридной би-резонансной наноантенной

3 Связь между спонтанным параметрическим рассеянием и генерацией второй гармоники

Заключение

5 Перечень графического материала (с указанием обязательного материала)

Данная ВКР включает 26 рисунков

6 Исходные материалы и пособия

1. “Generation of Photon-Plasmon Quantum States in Nonlinear Hyperbolic Metamaterials” / Poddubny A.N., Iorsh I.V., Sukhorukkov A.A. //Physical Review Letters. — 2016. — Vol. 117, no. 12. — Pp. 1–6.

2. “Second-harmonic generation in Mie-resonant dielectric nanoparticles made of noncentrosymmetric materials” / Kristina Frizyuk, Irina Volkovskaya, Daria Smirnova et al. //Physical Review B. — 2019. — Vol. 99, no. 7. — Pp. 1–18

3. “Reshaping the Second-Order Polar Response of Hybrid Metal–Dielectric Nanodimers” / Claude Renaut, Lukas Lang, Kristina Frizyuk et al. //Nano Letters. — 2019. — Vol. 19, no. 2. — Pp. 877–884

4. “Absorption and Scattering of Light by Small Particles” / C. Bohren, D. R. Huffman //Wiley Science Paperback Series, 1998.

5. “Spontaneous photon-pair generation from a dielectric nanoantenna” / Giuseppe Marino, Alexander S. Solntsev, Lei Xu et al. //Optica. — 2019. — Nov. — Vol. 6, no. 11. — Pp. 1416–1422

7 Дата выдачи задания « 10 » « декабря » 2019 г.

Руководитель ВКР Петров Михаил Игоревич
(ФИО)

Ministry of Science and Higher Education of the Russian Federation

ITMO University

**SUMMARY
OF A GRADUATION THESIS**

Student Anna A. Nikolaeva

Title of the thesis Second-order nonlinear processes in all-dielectric and hybrid metal-dielectric nanostructures

Name of organization ITMO University

DESCRIPTION OF THE GRADUATION THESIS

1 Research objective

Study the spontaneous parametric down-conversion of light by resonant spherical dielectric nanoparticle and second harmonic generation by bi-resonant hybrid metal-dielectric nanoantenna.

2 Research tasks

1) Apply two-photon amplitude method to describe spontaneous parametric down-conversion of light by a dielectric nanoparticle in the Mie configuration.

2) Investigate spatial correlations between signal and idler photons, plot radiation patterns for collinear decay;

3) Explore polarization correlations between signal and idler photons.

4) Find such parameters of the hybrid Au-BTO nanoantenna, that there is a localized surface plasmon resonance at the fundamental frequency, and a Mie resonance is present at the SHG frequency.

5) Obtain the spectrum of the SHG efficiency of the hybrid Au-BTO nanoantenna and receive the increase in the generation efficiency relative to an individual BTO nanoparticle.

6) Investigate the generation efficiency with respect to various parameters of the system, such as the position of the particle, the orientation of the crystal lattice and the polarization of the incident field, and compare it with experiment.

3 Number of sources listed in the review section 48

4 Total number of sources used in the thesis 67

5 Sources by years:

| Russian | | | Foreign | | |
|---------------------|---------------|--------------------|---------------------|---------------|--------------------|
| In the last 5 years | 5 to 10 years | More than 10 years | In the last 5 years | 5 to 10 years | More than 10 years |
| | | | 47 | 12 | 8 |

6 Use of online (internet) resources No

7 Use of modern computer software suites and technologies (List which ones were used and for which section of the thesis)

| Software suites and technologies | Thesis section |
|----------------------------------|----------------|
| Matlab R2016b | 2,3 |
| COMSOL Multiphysics 5.5 | 3 |

8 Short summary of results/conclusions

In this work, we investigated two second-order nonlinear processes — spontaneous parametric down-conversion (SPDC) and second-harmonic generation (SHG). It was confirmed that these processes are reverse and have the same selection rules, depending on the particle and the orientation of the crystalline lattice. For SPDC from a resonant dielectric spherical nanoparticle, we obtained the expression for the two-photon amplitude in terms of vector spherical harmonics. Then we examined the spatial and polarization correlations between the signal and idler photons and obtained directed nonlinear emission of the photons and the condition on it, similar to the linear Kerker effect. For SHG from a bi-resonant hybrid nanoantenna, consisting of a spherical particle of barium titanate BTO and a gold dimer nanoantenna, we selected the antenna parameters such that enhancement of the SHG occurs due to plasmon resonance at the fundamental wavelength and Mie resonance at the second harmonic wavelength. An increase in the SHG efficiency by three orders of magnitude relative to a single barium titanate particle was obtained numerically and experimentally. We also found that the SHG efficiency strongly depends on the orientation of the crystalline lattice, the position of the barium titanate particle and the polarization of the incident field.

9 Grants received while working on the thesis _ Competition of scientific projects to support students working in the field of quantum technologies from the Center for Quantum Technologies at Moscow State University.

10 Have you produced any publications or conference reports on the topic of the thesis? Yes

- a) 1) Petrov M.I., Nikolaeva A.A., Frizyuk K.S., Olekhno N.A. Second harmonic generation and spontaneous parametric down-conversion in Mie nanoresonators // Journal of Physics: Conference Series – 2018, Vol. 1124, pp. 051021

(Bibliographical description of a publication)

- b) 1) Nikolaeva A.A. , “Directional two-photon emission by a resonant nanoparticle in the SPDC process”, METANANO 2019, 15-19 July 2019, Saint-Petersburg, Russia. (poster).

(Bibliographical description of a conference report)

АННОТАЦИЯ

ВЫПУСКНОЙ КВАЛИФИКАЦИОННОЙ РАБОТЫ

Обучающийся Николаева Анна Андреевна

Наименование темы ВКР: Нелинейные процессы второго порядка в диэлектрических и гибридных металл-диэлектрических наноструктурах

Наименование организации, где выполнена ВКР Университет ИТМО

ХАРАКТЕРИСТИКА ВЫПУСКНОЙ КВАЛИФИКАЦИОННОЙ РАБОТЫ

1 Цель исследования

Изучение спонтанного параметрического рассеяния света резонансной диэлектрической сферической наночастицей и генерации второй гармоники от би-резонансной гибридной металл-диэлектрической наноантенны

2 Задачи, решаемые в ВКР

- 1) Применить аппарат двухфотонной амплитуды для описания спонтанного параметрического рассеяния света диэлектрической наночастицей в конфигурации Ми.
- 2) Исследовать пространственные корреляции между сигнальным и холостым фотонами, построить диаграммы направленности излучения для коллинеарного распада.
- 3) Исследовать поляризационные корреляции между сигнальными и холостыми фотонами.
- 4) Подобрать такие параметры гибридной наноантенны Au-ВТО, чтобы на основной частоте имелся локализованный поверхностный плазмонный резонанс, а на частоте ГВГ присутствовал Ми резонанс.
- 5) Получить спектр эффективности ГВГ гибридной наноантенны Au-ВТО и определить увеличение эффективности генерации относительно отдельной наночастицы ВТО.
- 6) Исследовать зависимость эффективности генерации второй гармоники от различных параметров системы, таких как положение частицы, ориентация кристаллической решетки и поляризация падающего поля. Сравнить полученные результаты с экспериментом.

2 Число источников, использованных при составлении обзора 48

4 Полное число источников, использованных в работе 67

5 В том числе источников по годам

| Отечественных | | | Иностраных | | |
|-----------------|----------------|--------------|-----------------|----------------|--------------|
| Последние 5 лет | От 5 до 10 лет | Более 10 лет | Последние 5 лет | От 5 до 10 лет | Более 10 лет |
| | | | 47 | 12 | 8 |

6 Использование информационных ресурсов Internet нет

7 Использование современных пакетов компьютерных программ и технологий (Указать, какие именно, и в каком разделе работы)

| Пакеты компьютерных программ и технологий | Раздел работы |
|---|---------------|
| Matlab 2016b | 2,3 |
| COMSOL Multiphysics 5.5 | 3 |

8 Краткая характеристика полученных результатов

В данной работе мы исследовали два нелинейных процесса второго порядка – спонтанное параметрическое рассеяние (СПР) и генерация второй гармоники (ГВГ). Получили подтверждение, что эти процессы являются обратными и имеют одинаковые правила отбора, зависящие от частицы и ориентации кристаллической решетки. Для СПР от резонансной сферической наночастицы мы получили выражение для двухфотонной амплитуды через векторные сферические гармоники. Затем мы исследовали пространственные и поляризационные корреляции между сигнальным и холостым фотонами и получили направленное нелинейное испускание фотонов и условие на него, аналогично линейному эффекту Керкера. Для ГВГ от би-резонансной гибридной наноантенны, состоящей из сферической частицы титаната бария ВТО и золотой димерной антенны, мы подобрали параметры антенны такие, что усиление генерации второй гармоники происходит за счет плазмонного резонанса на фундаментальной длине волны и Ми резонанса на длине волны второй гармоники. Численно и экспериментально получено усиление эффективности ГВГ на три порядка относительно одиночной частицы титаната бария. Так же мы получили, что эффективность ГВГ сильно зависит от ориентации кристаллической решетки, положения частицы титаната бария и поляризации падающего поля.

9 Полученные гранты, при выполнении работы Конкурс научных проектов для поддержки аспирантов и студентов, работающих в области квантовых технологий от Центра квантовых технологий МГУ.

10 Наличие публикаций и выступлений на конференциях по теме выпускной работы да

a) 1) Petrov M.I., Nikolaeva A.A., Frizyuk K.S., Olekhno N.A. Second harmonic generation and spontaneous parametric down-conversion in Mie nanoresonators // Journal of Physics: Conference Series – 2018, Vol. 1124, pp. 051021

(Библиографическое описание публикаций)

б) 1) Николаева А.А. “Directional two-photon emission by a resonant nanoparticle in the SPDC process”, Международная конференция METANANO 2019, 15-19 июля 2019, Санкт-Петербург, Россия. (постер)

(Библиографическое описание выступлений на конференциях)

CONTENTS

| | |
|--|----|
| INTRODUCTION | 9 |
| 1 METHODS | 15 |
| 1.1 Two-photon amplitude | 15 |
| 1.2 Mie theory | 16 |
| 1.3 Numerical simulation | 20 |
| 1.4 Green function for dielectric sphere | 22 |
| 1.5 Non-linear materials: BaTiO ₃ , GaAs | 23 |
| 2 SPONTANEOUS PARAMETRIC DOWN-CONVERSION BY DIELECTRIC NANOPARTICLE | 26 |
| 2.1 Linear Kerker effect | 26 |
| 2.2 Non-linear generation of entangled photons | 28 |
| 2.3 Directional emission from GaAs nanoparticle | 31 |
| 2.3.1 Forward/backward directivity | 33 |
| 2.3.2 Generalized directivity conditions | 37 |
| 2.4 Polarization correlations | 38 |
| 3 SECOND HARMONIC GENERATION BY HYBRID METAL-DIELECTRIC NANOANTENNA | 40 |
| 3.1 Analysis of the resonance properties of a hybrid nanoantenna | 41 |
| 3.1.1 Scattering on a BaTiO ₃ spherical nanoparticle . | 41 |
| 3.1.2 Scattering on a gold nanodimer | 42 |
| 3.1.3 Scattering on a hybrid bi-resonance nanoantenna | 43 |
| 3.2 Second harmonic generation efficiency of a hybrid bi- resonance nanoantenna | 44 |
| 3.2.1 The influence of the crystalline lattice orientation | 45 |
| 3.2.2 The influence of the particle position | 45 |
| 3.2.3 Experimental measurement of scattering spectra | 47 |
| 3.2.4 Experimental measurement of second harmonic generation efficiency | 49 |
| 4 CONNECTION BETWEEN SPONTANEOUS PARAMETRIC DOWN-CONVERSION AND SECOND HARMONIC GENERATION | 55 |

| | |
|----------------------|----|
| CONCLUSION | 57 |
| REFERENCES | 59 |
| APPENDIX A | 67 |
| APPENDIX B | 71 |

INTRODUCTION

For the last several decades, the constant demand on downscaling the optical devices drives the development of nanophotonics. One of the main interest of the researches lies in inventing novel active systems for light emission. Though, the strong progress in subwavelength lasing structures has been recently shown [1], the efficient nanoscale nonlinear optical operating on high-harmonic generation regime were still inaccessible due to intrinsically low efficiency of this process and spatial restrictions, which do restrict phase matching effects. The plasmonic nanostructures were considered as main candidates for efficient subwavelength nonlinear sources due to their strong field enhancement [2]. However, strong optical losses and weak nonlinearity limit the efficiency of nonlinear generation. Recently, the all-dielectric nanostructures have been suggested as efficient resonant subwavelength systems [3, 4]. Possessing the lower order Mie resonances [5, 6] they became attractive for various photonics applications including nonlinear photonics [7].

In the prospective of nonlinear photonics, the all-dielectric structures have demonstrated very high efficiency of third order processes such as third harmonic generation [8, 9, 10] and Kerr nonlinearity [11, 12]. The absence of the losses in all-dielectric structures together with strong mode localization in the volume of the resonators became the basic features responsible for the strong nonlinear response. Nonlinear effects are described by expanding the polarization of a substance in powers of the electric field that excites this polarization:

$$P_i = \chi_{ij}^{(1)} E_j + \chi_{ijk}^{(2)} E_j E_k + \chi_{ijkl}^{(3)} E_j E_k E_l + \dots,$$

where P_i and E_i are the components of the polarization and electric field vectors with the index i , $\chi^{(n)}$ is the n^{th} order nonlinear susceptibility tensor. The first term in this expansion is responsible for the linear effects associated with the polarization of matter. The second term is responsible for second-order nonlinear processes, in particular, second harmonic generation (SHG), is a process in which two photons with the same frequency ω interact with a nonlinear material and generate a

new photon with twice frequency 2ω , and spontaneous parametric down-conversion, is a process that converts one photon of higher frequency ω_p (namely, a pump photon), into a pair of photons (namely, a signal photon, and an idler photon) of lower frequencies, in accordance with the law of conservation of energy $\hbar\omega_p = \hbar\omega_i + \hbar\omega_s$.

Second harmonic generation by plasmon nanostructures

Nowadays, the most common resonant nanosystems are metal (plasmon) nanostructures [13]. The presence of free electrons in metals makes it possible to observe localized surface plasmon resonances in nanoparticles much smaller than the wavelength. Multiple enhancement of local electric fields also leads to increased the nonlinear effects in plasmonics [14]. On the other hand, an important disadvantage of plasmon systems is the central symmetry of the crystal structure of metals, and, consequently, the absence of the tensor $\chi^{(2)}$ in the volume of metals. However, metal nanoparticles with plasmon resonances demonstrate second-harmonic generation [2]. This occurs due to two effects: a) surface - local inverse symmetry is removed near the surface, due to which a nonzero surface tensor $\chi^{(2)}$ can arise; b) bulk — the presence of spatial inhomogeneity of the fields inside a particle can also lead to the generation of the second harmonic due to additional terms containing gradient fields in the expansion of polarization. These two mechanisms make the main contribution to SHG from nanostructures made of materials with an inversion center. These generation mechanisms are rather weak, which requires new approaches to enhance generation. So, in particular, approaches are proposed for the use of bi-resonance plasmon structures that have resonance both at the fundamental frequency and at the second harmonic frequency [15, 16]. Nevertheless, the characteristic experimentally measured value of the generation efficiency for single plasmon structures is about $10^{-9} - 10^{-8}$ [17]. Such a small value of this quantity is primarily associated with small values of the second order nonlinear tensor $\chi^{(2)}$ in metals, as well as the low quality factor of plasmon systems with high ohmic losses.

Second harmonic generation by nonmetallic nanostructures

A possible alternative to plasmon nanostructures as subwavelength resonators is dielectric resonance nanostructures with a high refractive index. Recently, much attention has been paid to the study of such nanoresonators [3, 18]. This is due to the fact that the resonances of both electric and magnetic modes are well pronounced for such structures with sizes much smaller than the wavelength in vacuum. This, along with the electrical response of the system, also provides an artificial magnetic response, allowing independent control of the electric and magnetic components of the electromagnetic field at the nanoscale.

An important advantage of nonmetallic nanostructures in comparison with metallic ones is a wide selection of materials of dielectrics and semiconductors, which, on the one hand, have a sufficiently high refractive index and, on the other hand, demonstrate various optical properties due to the variety of crystal systems. One of the main materials that are proposed to be used for the implementation of such dielectric resonators is silicon, whose refractive index is about ~ 4 [19] in the optical range. In this case, silicon does not have significant optical losses up to a wavelength of 600 nm. However, silicon is not an optimal material for SHG, since it has an inversion center, and, similarly to plasmon structures, the generation occurs due to surface effects and due to field gradients in the bulk. Nevertheless, SHG from such structures was observed experimentally [20].

However, along with silicon, there are a large number of other dielectric and semiconductor materials that do not have an inversion center, which ensures their high SHG efficiency. Recent studies have shown that due to Mie resonances in subwavelength structures, SHG can be significantly enhanced, for example, in BaTiO₃ [21] nanoparticles, AlGaAs [22, 23] and GaP [24] nanodisks. The works of [25] demonstrated that the generation efficiency in such systems can reach values of $10^{-5} - 10^{-4}$, which is many orders of magnitude higher than the values for metal nanostructures. Further development of this approach allows the creation

of nonlinear metasurfaces (periodic structures with a period shorter than the wavelength), which make it possible to efficiently generate and control the polarization of the second harmonic [26]. Recent theoretical calculations [27] and later experimental realization [28] showed that it is possible to achieve generation efficiency up to 0.1 % . Besides high-efficiency of the SHG emission the all-dielectric structures allow for manipulation over the directionality of the nonlinear emission [29, 30].

Spontaneous parametric down-conversion

Along with the second harmonic generation, of strong interest is the inverse nonlinear process of photon pairs generation through spontaneous parametric down-conversion process (SPDC), which is one of the most common mechanism of entangled quantum state creation. Generation of entangled photons and their correlation measurements became one of the central topics in quantum optics addressing the fundamental aspects of quantum mechanics and driving the development of novel solutions in quantum technologies [31, 32]. By now, the generation of entangled photons has been successfully downscaled from free space experiments to on-chip dielectric waveguides [33] enabling integrated quantum photonics applications ranging from quantum information (processing) [34] to spectroscopy [35].

In this prospective, the further downscaling of the entangled photons generation became one of the topical problems in quantum nanophotonics. Many approaches base on utilization of plasmonic nanostructures for enhancing entangled photons generation from various solid state quantum sources [36, 37, 38, 39]. However, these approaches require cryogenic temperatures for reaching stable emission of entangled photons. The SPDC sources do not have these restrictions. A significant progress in this field of SPDC generation from subwavelength structures was achieved recently and reported in Ref. [40], where the researchers have measured the SPDC of photon from a single AlGaAs disk supporting lower Mie resonances. Despite of that, the comprehensive theory of SPDC

process enhanced by multipolar resonances in nanostructures has not been proposed and that was one of the main tasks of the current work.

Hybrid metal–dielectric structures

Alternative approach to nanophotonic structures design bases on mixing the properties of all-dielectric and plasmonic systems. Strong field enhancement in small volumes typical for plasmonics structures together with directional light emission provided by electric and magnetic response of dielectric structures can be combined in the so-called *hybrid* metal–dielectric structures. The linear optical properties related to dipole coupling in such systems have been considered in the papers [41, 42, 43, 44].

The approach to hybrid photonic structures was also suggested for enhancing the nonlinear optical properties such as second harmonic generation. Different nanoscale system were suggested, such as core-shell structures [45] and dipolar plasmonics nanoantenna structures [43, 46], nanoparticle dimers [21, 47] as well as layered disks structures [48]. Of special interest is the paper by Stefan Linden group [43] which proposes utilization of double resonant plasmonic antenna for light enhancement both at the fundamental and second harmonic frequencies. However, both resonances were provided by the plasmonic structures while the dielectric counterpart had no resonances in the visible range. This work is aimed at combining Mie and plasmonic resonance to achieve double enhancement of the SHG both at the fundamental and second harmonic wavelengths.

The aim of the work

Basing on the analysis of the recent developments in the field of Mie resonant nonlinear nanophotonics, we have identified double-folded **aims of our work:**

1) theoretical study of spontaneous parametric down-conversion of light, enhanced by resonances of a dielectric spherical nanoparticle with bulk

non-linearity $\chi_{bulk}^{(2)}$. To achieve this goal it is necessary to solve the following tasks:

- apply two-photon amplitude method to describe spontaneous parametric down-conversion of light by a dielectric nanoparticle in the Mie configuration;
- investigate spatial correlations between signal and idler photons and far-field photons generation patterns for collinear decay;
- explore polarization correlations between signal and idler photons.

2) *numerically and experimental study of second harmonic generation by hybrid bi-resonant Au-BaTiO₃ nanoantenna*. To achieve this goal it is necessary to solve the following tasks:

- identify the parameters of the hybrid Au-BaTiO₃ nanosystem providing the localized surface plasmon resonance at the fundamental frequency ω , and Mie resonance present at the doubled frequency 2ω ;
- obtain the spectrum of the SHG efficiency of the hybrid Au-BaTiO₃ nanoantenna and receive the increase in the generation efficiency relative to an individual BaTiO₃ nanoparticle;
- investigate the generation efficiency with respect to various parameters of the system, such as the position of the particle, the orientation of the crystal lattice and the polarization of the incident field, and compare it with the experiment.

1 METHODS

This section will discuss the basic methods and approaches that have been used in the work. In particular, the two-photon amplitude method [49], the Mie theory of scattering on a dielectric sphere [50], the dyadic Green function for the dielectric sphere [51] and numerical simulations in Comsol Multiphysics.

1.1 Two-photon amplitude

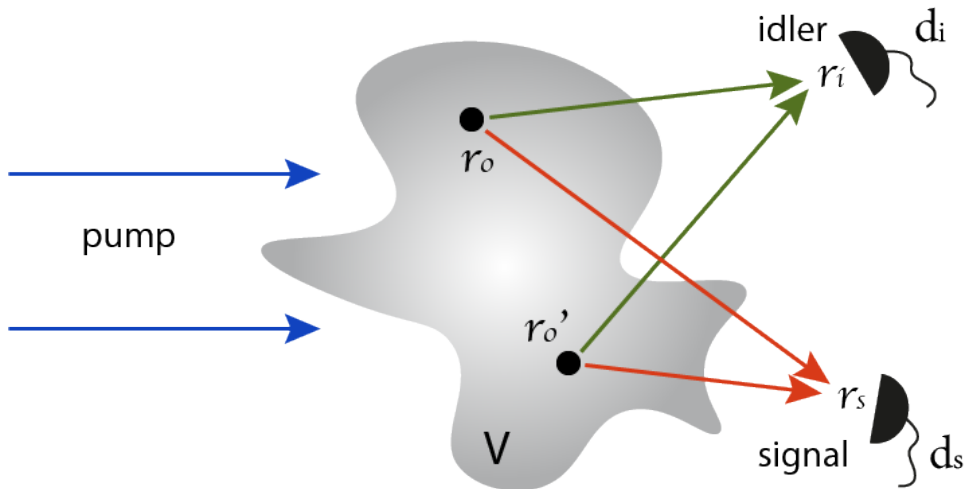


Figure 1.1 — Scheme of the photon-pair generation from a nonlinear material

To solve the problems, we used the approach of two-photon amplitude [49], where the generation of photon pairs from an incident pump wave on a dielectric structure was theoretically studied (see Figure 1.1). One of the key results of this consideration was the two-photon amplitude, which shows the probability of detecting correlated photons (bi-photons):

$$T_{is}(\mathbf{r}_i, \omega_i, \mathbf{d}_i; \mathbf{r}_s, \omega_s, \mathbf{d}_s) = \int_V \langle \mathbf{d}_i^* | \hat{G}(\mathbf{r}_i, \mathbf{r}_0, \omega_i) \hat{\Gamma}(\mathbf{r}_0) \hat{G}(\mathbf{r}_0, \mathbf{r}_s, \omega_s) | \mathbf{d}_s^* \rangle d^3 r_0, \quad (1.1)$$

where integration is performed over the generation nonlinear domain V , \mathbf{d}_i , \mathbf{d}_s — detector's dipole moments, \hat{G} — dyadic Green function of the system, $\hat{\Gamma}$ — generation matrix. In our study, we considered the SPDC

process by a nanoparticle associated with the presence of a second-order nonlinear susceptibility tensor $\chi^{(2)}$. For such a process the generation matrix has the form

$$\hat{\Gamma}_{\alpha\beta}(\mathbf{r}_0) = \chi_{\alpha\beta\gamma}^{(2)} \mathbf{E}_p^\gamma(\mathbf{r}_0), \quad (1.2)$$

where $\mathbf{E}_p(\mathbf{r}_0)$ – classical pump field inside a nanoparticle.

Coincidence rate defined by the expression

$$w_{is}(\mathbf{r}_i, \omega_i, \mathbf{d}_i; \mathbf{r}_s, \omega_s, \mathbf{d}_s) = \frac{2\pi}{\hbar} \delta(\hbar\omega_i + \hbar\omega_s - \hbar\omega_p) |T_{is}(\mathbf{r}_i, \omega_i, \mathbf{d}_i; \mathbf{r}_s, \omega_s, \mathbf{d}_s)|^2 \quad (1.3)$$

and has dimension $[\text{sm}^{-4}\text{s}^{-1}]$.

The probability of detecting two photons at given points in space is determined by the integral of the expression w_{is} over the areas of the detectors S_i, S_s and the measurement time τ :

$$P_{is} = \int_{S_i} \int_{S_s} \int_{\tau} w_{is} dS_i dS_s dt = w_{is} S_i S_s \tau$$

Thus, the probability of detecting two photons is proportional to the squared modulus of the two-photon amplitude $|T_{is}|^2$. In what follows, we assume that the areas of the detectors and the measurement time are unit, and, as a consequence, the values of w_{is} and P_{is} are numerically equal.

1.2 Mie theory

Consider the problem of elastic light scattering by spherical nanoparticles. A similar problem was solved in the framework of the Mie theory [50]. Based on Maxwell's equations, it can be obtained that the electromagnetic field in a linear isotropic homogeneous medium must satisfy the vector wave equations

$$\nabla^2 \mathbf{E} + k^2 \mathbf{E} = 0, \quad \nabla^2 \mathbf{H} + k^2 \mathbf{H} = 0, \quad k^2 = \frac{\omega^2}{c^2} \varepsilon \mu,$$

and have zero divergence:

$$\nabla \cdot \mathbf{E} = 0, \quad \nabla \cdot \mathbf{H} = 0.$$

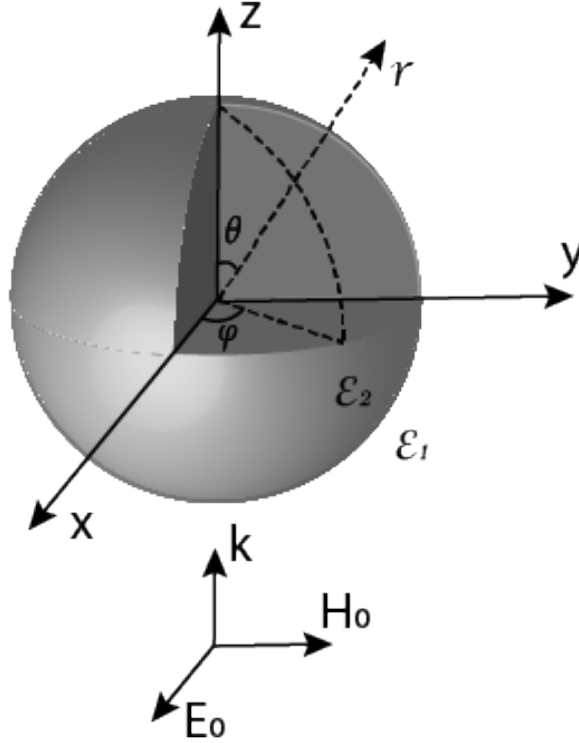


Figure 1.2 — Spherical polar coordinate system centered on a spherical particle of radius a . The plane wave incident on a spherical dielectric nanoparticle with $\varepsilon_2(\omega)$ from the medium with ε_1 , propagating along z - axis, and the electric field oscillates along x - axis

It is convenient to introduce a scalar function ψ that satisfies the scalar wave equation and is generating function for vector spherical harmonics \mathbf{M} and \mathbf{N} :

$$\mathbf{M} = \nabla \times (\mathbf{r}\psi), \quad \mathbf{N} = \frac{\nabla \times \mathbf{M}}{k}.$$

The functions \mathbf{M} and \mathbf{N} possess all the necessary properties of the electromagnetic field, namely: they satisfy the vector wave equation, their divergence is zero, the curl \mathbf{M} is proportional to \mathbf{N} , and the curl \mathbf{N} is proportional to \mathbf{M} :

$$\nabla \cdot \mathbf{M} = 0, \quad \nabla \cdot \mathbf{N} = 0, \quad \nabla \times \mathbf{M} = k\mathbf{N}, \quad \nabla \times \mathbf{N} = k\mathbf{M}$$

Thus, the problem reduces to finding solutions of the scalar wave equation, and the vector harmonics \mathbf{M} and \mathbf{N} in spherical coordinates

have the following form [50]:

$$\begin{aligned} \mathbf{M}_{emn}(k, \mathbf{r}) = & -\frac{m}{\sin \theta} \sin m\varphi \cdot P_n^m(\cos \theta) z_n(\rho) \mathbf{e}_\theta - \\ & - \cos m\varphi \cdot \frac{dP_n^m(\cos \theta)}{d\theta} z_n(\rho) \mathbf{e}_\varphi \end{aligned} \quad (1.4)$$

$$\begin{aligned} \mathbf{M}_{omn}(k, \mathbf{r}) = & \frac{m}{\sin \theta} \cos m\varphi \cdot P_n^m(\cos \theta) z_n(\rho) \mathbf{e}_\theta - \\ & - \sin m\varphi \cdot \frac{dP_n^m(\cos \theta)}{d\theta} z_n(\rho) \mathbf{e}_\varphi \end{aligned} \quad (1.5)$$

$$\begin{aligned} \mathbf{N}_{emn}(k, \mathbf{r}) = & \frac{z_n(\rho)}{\rho} \cos m\varphi \cdot n(n+1) P_n^m(\cos \theta) \mathbf{e}_r + \\ & + \cos m\varphi \cdot \frac{dP_n^m(\cos \theta)}{d\theta} \frac{1}{\rho} \frac{d}{d\rho} [\rho z_n(\rho)] \mathbf{e}_\theta - \\ & - m \sin m\varphi \cdot \frac{P_n^m(\cos \theta)}{\sin \theta} \frac{1}{\rho} \frac{d}{d\rho} [\rho z_n(\rho)] \mathbf{e}_\varphi \end{aligned} \quad (1.6)$$

$$\begin{aligned} \mathbf{N}_{omn}(k, \mathbf{r}) = & \frac{z_n(\rho)}{\rho} \sin m\varphi \cdot n(n+1) P_n^m(\cos \theta) \mathbf{e}_r + \\ & + \sin m\varphi \cdot \frac{dP_n^m(\cos \theta)}{d\theta} \frac{1}{\rho} \frac{d}{d\rho} [\rho z_n(\rho)] \mathbf{e}_\theta + \\ & + m \cos m\varphi \cdot \frac{P_n^m(\cos \theta)}{\sin \theta} \frac{1}{\rho} \frac{d}{d\rho} [\rho z_n(\rho)] \mathbf{e}_\varphi, \end{aligned} \quad (1.7)$$

where $n = 0, 1, 2, 3, \dots$, $m = 0, \dots, n$, the indices e and o denote even and odd linearly independent solutions for ψ along the azimuthal angle φ , in place of $z_n(\rho)$, where $\rho = kr$ is the dimensionless variable, can be Bessel $j_n(\rho)$ or Hankel $h_n^{(1)}(\rho)$ spherical functions, depending on the specific boundary conditions; P_n^m - associated Legendre polynomials:

$$\begin{aligned} P_0^0 &= 1, \\ P_1^0 &= x = \cos \theta, \\ P_1^1 &= \sqrt{(1-x^2)} = \sin \theta, \\ P_2^0 &= \frac{1}{2}(3x^2 - 1) = \frac{1}{4}(1 + \cos 2\theta), \dots \end{aligned}$$

Suppose that a x -polarized plane wave is incident on a homogeneous isotropic sphere of radius a (Figure 1.2). The incident, internal and scattered fields are represented in the form of expansion in vector

spherical harmonics, and the corresponding expansion coefficients are found from the boundary conditions:

$$(\mathbf{E}_i + \mathbf{E}_s - \mathbf{E}_1) \times \mathbf{e}_r = (\mathbf{H}_i + \mathbf{H}_s - \mathbf{H}_1) \times \mathbf{e}_r = 0,$$

where $\mathbf{E}_i, \mathbf{E}_s, \mathbf{E}_p$ — incident, scattered and internal fields, respectively. For the incident field and the field inside the particle, vector spherical harmonics are used, in which the radial dependence of the generating functions is determined by the Bessel spherical functions $j_n(\rho)$. For a scattered field — Hankel spherical functions $h_n^{(1)}(\rho)$ are used, hereinafter, superscript (1), corresponding to a diverging spherical wave. The field inside the particle, further the pump field in equation 1.1, has the form

$$\mathbf{E}_p(k, \mathbf{r}) = \sum_{n=1}^{\infty} E_n (c_n \mathbf{M}_{o1n}(k, \mathbf{r}) - id_n \mathbf{N}_{e1n}(k, \mathbf{r})), \quad (1.8)$$

$$E_n = i^n E_0 \frac{2n+1}{n(n+1)},$$

where E_0 — the incident field modulus, and the coefficients c_n and d_n in the expansion in vector spherical harmonics have a resonant frequency dependence and are presented in the following form:

$$c_n = \frac{j_n(\rho_1)[\rho_1 h_n^{(1)}(\rho_1)]' - h_n^{(1)}(\rho_1)[\rho_1 j_n(\rho_1)]'}{j_n(\rho_2)[\rho_1 h_n^{(1)}(\rho_1)]' - \frac{\mu_1}{\mu_2} h_n^{(1)}(\rho_1)[\rho_2 j_n(\rho_2)]'}, \quad (1.9)$$

$$d_n = \frac{j_n(\rho_1)[\rho_1 h_n^{(1)}(\rho_1)]' - h_n^{(1)}(\rho_1)[\rho_1 j_n(\rho_1)]'}{\frac{\mu_1}{\mu_2} \frac{k_2}{k_1} j_n(\rho_2)[\rho_1 h_n^{(1)}(\rho_1)]' - \frac{k_1}{k_2} h_n^{(1)}(\rho_1)[\rho_2 j_n(\rho_2)]'}, \quad (1.10)$$

$$\rho_1 = k_1 a = \frac{2\pi a}{\lambda}, \quad \rho_2 = k_2 a = \frac{2\pi a \sqrt{\varepsilon_2 \mu_2}}{\lambda},$$

where a is the radius of the sphere, and k_1 and k_2 are the wave numbers outside and inside the sphere, respectively. Dielectric permittivity of surrounding media $\varepsilon_1 = 1$, dielectric permittivity of the sphere $\varepsilon_2(\omega)$. Magnetic permeability outside the sphere μ_1 and magnetic permeability of the nanoparticle μ_2 , further we consider them equal to 1.

The scattered field decomposed into vector spherical harmonics can be represented as

$$\mathbf{E}_s(k, \mathbf{r}) = \sum_{n=1}^{\infty} E_n (i a_n \mathbf{N}_{e1n}^{(1)}(k, \mathbf{r}) - b_n \mathbf{M}_{o1n}^{(1)}(k, \mathbf{r})), \quad (1.11)$$

where the coefficients a_n and b_n are determined by the expressions

$$a_n = \frac{\frac{\mu_1}{\mu_2} \left(\frac{k_2}{k_1}\right)^2 j_n(\rho_2) [\rho_1 j_n(\rho_1)]' - j_n(\rho_1) [\rho_2 j_n(\rho_2)]'}{\frac{\mu_1}{\mu_2} \left(\frac{k_2}{k_1}\right)^2 j_n(\rho_2) [\rho_1 h_n^{(1)}(\rho_1)]' - h_n^{(1)}(\rho_1) [\rho_2 j_n(\rho_2)]'}, \quad (1.12)$$

$$b_n = \frac{j_n(\rho_2) [\rho_1 j_n(\rho_1)]' - \frac{\mu_1}{\mu_2} j_n(\rho_1) [\rho_2 j_n(\rho_2)]'}{j_n(\rho_2) [\rho_1 h_n^{(1)}(\rho_1)]' - \frac{\mu_1}{\mu_2} h_n^{(1)}(\rho_1) [\rho_2 j_n(\rho_2)]'}. \quad (1.13)$$

The coefficients a_n and b_n in the expansion of the scattered field (eq. 1.11) have the same denominator as the coefficients c_n and d_n in the expansion of the field inside the particle (eq. 1.8), that is, they have resonances at the same values frequencies.

The scattering cross section corresponds to the obtained field distribution has the form:

$$\sigma_{scat} = \frac{2\pi}{k^2} \sum_{n=1}^{\infty} (2n+1) (|a_n|^2 + |b_n|^2) \quad (1.14)$$

In fact, the series (eq. 1.14) is a multipole expansion, where a_1 and b_1 correspond to the electric and magnetic dipole modes contribution, respectively, a_2 and b_2 correspond to the electric and magnetic quadrupole modes contribution and so on.

1.3 Numerical simulation

To describe the interaction of light with nanoparticles, we used the scattering cross section σ_{scat} , which shows how much of the energy of the incident light was re-scattered by the system.

$$\sigma_{scat} = \frac{P_{scat}}{|\mathbf{S}_{inc}|}, \quad (1.15)$$

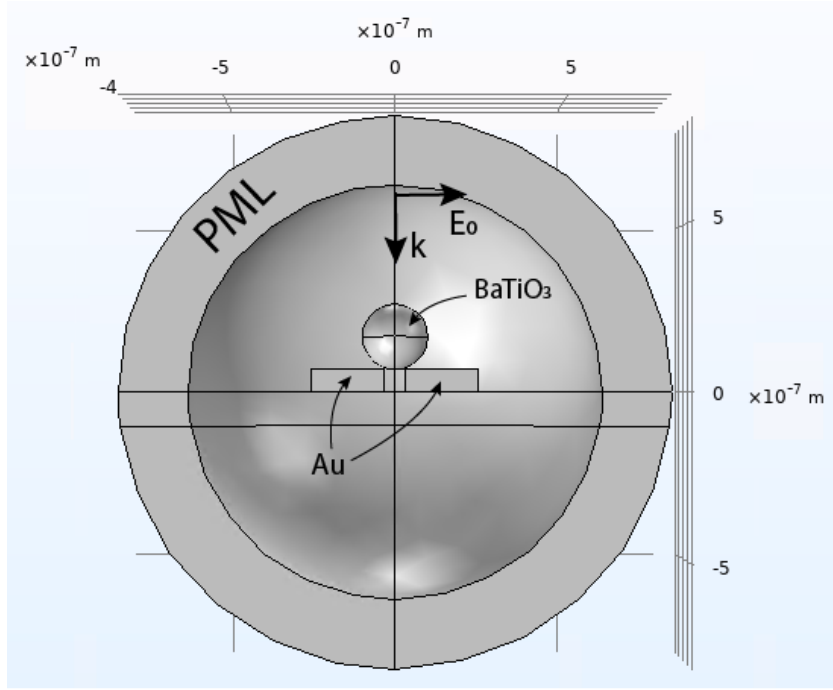


Figure 1.3 — View of the domain of numerical solution of the problem in Comsol Multiphysics

where P_{scat} — scattered field power, \mathbf{S}_{inc} — Pointing vector of incident wave. To get scattering efficiency we normalized the corresponding cross section to geometrical cross section.

$$\eta_{scat} = \frac{\sigma_{scat}}{\sigma_{geom}} \quad (1.16)$$

SHG efficiency is measured in [1/W] and is defined as follows:

$$\eta_{SHG} = \frac{P_{SHG}}{P_{inc}^2}, \quad (1.17)$$

where P_{SHG} — second harmonic generation power and P_{inc} — incident power. Subsequently, all SHG spectra were obtained for plane waves with amplitude $E_0 = 10^8$ V/m, which corresponds to the incident light intensity $I \simeq 10^{12}$ W/m².

The scattering problem on hybrid Au-BaTiO₃ nanoantenna in our configuration has no analytical solution (Figure 1.3). To find the scattering cross section, in this case, a Comsol Multiphysics numerical simulation package was used. We set the initial conditions, a plane wave propagating in the opposite direction to the z-axis and the electric field oscillates along the y-axis. Then, in a given area (Figure 1.3), the equation

obtained directly from the Maxwell equations is solved by the finite element method (FEM):

$$\nabla \times \frac{1}{\mu} \nabla \times \mathbf{E} - k_0^2 \left(\varepsilon - \frac{i\sigma}{\omega \varepsilon_0} \right) \mathbf{E} = 0,$$

where $k_0 = \omega/c$, μ – magnetic permeability, ε – dielectric permittivity, ε_0 – vacuum permittivity, σ – conductivity. At the boundary of the region, the deceduous field should be represented as the sum of a spherical and plane wave; to fulfill this condition, the model was surrounded by Perfect Matched Layer (PML) as it shown in the Figure 1.3. After finding the distribution of the electric field, it is not difficult to numerically calculate all the quantities that we need, such as the power and cross section of the scattering (eq. 1.15).

To simulate the second harmonic generation, we introduced bias currents inside the BaTiO₃ nanoparticle induced by nonlinear polarization

$$\mathbf{j}_{2\omega} = \frac{\partial \mathbf{P}_{2\omega}}{\partial t} = i2\omega \mathbf{P}_{2\omega}, \quad (1.18)$$

where $P_{2\omega,i} = \varepsilon_0 \chi_{ijk}^{(2)} E_{\omega}^j E_{\omega}^k$, E_{ω}^k is k-th component of the electric field \mathbf{E}_{ω} on the fundamental frequency inside nanoparticle.

1.4 Green function for dielectric sphere

The dyadic Green function of the system, consisting of a dielectric sphere with $\varepsilon_2(\omega)$ and surrounding media with $\varepsilon_1 = 1$, similarly to the field inside, can be decomposed into vector spherical harmonics. Such an expansion is given in [51], where the following system of equations is solved to find the Green function:

$$\begin{cases} \nabla \times \nabla \times \hat{G}(\mathbf{r}, \mathbf{r}', \omega) - k_1^2 \hat{G}(\mathbf{r}, \mathbf{r}', \omega) = \hat{1} \delta(\mathbf{r} - \mathbf{r}'), & r \geq a \\ \nabla \times \nabla \times \hat{G}(\mathbf{r}, \mathbf{r}', \omega) - k_2^2 \hat{G}(\mathbf{r}, \mathbf{r}', \omega) = 0, & r \leq a \end{cases}$$

$$k_1 = \frac{\omega}{c} n_1 = \frac{\omega \sqrt{\varepsilon_1}}{c} \text{ – wave number outside nanoparticle,}$$

$$k_2 = \frac{\omega}{c} n_2 = \frac{\omega \sqrt{\varepsilon_2(\omega)}}{c} n \text{ – wave number inside nanoparticle.}$$

According to (eq. 1.1), we need that part of the Green function for which the source \mathbf{r}' is inside nanoparticle and the observation point \mathbf{r} is outside:

$$\hat{\mathbf{G}}^{(12)}(\mathbf{r}, \mathbf{r}', \omega) = \frac{ik_2}{4\pi} \sum_{n=1}^{\infty} \sum_{m=0}^n (2 - \delta_0) \frac{2n+1}{n(n+1)} \frac{(n-m)!}{(n+m)!} \cdot [a_n^{(2)} \mathbf{M}_{e_{mn}}^{(1)}(k_1, \mathbf{r}) \otimes \mathbf{M}_{e_{mn}}(k_2, \mathbf{r}') + b_n^{(2)} \mathbf{N}_{e_{mn}}^{(1)}(k_1, \mathbf{r}) \otimes \mathbf{N}_{e_{mn}}(k_2, \mathbf{r}')], \quad r > a > r' \quad (1.19)$$

$$\delta_0 = \begin{cases} 1, & m = 0 \\ 0, & m \neq 0 \end{cases},$$

where coefficients $a_n^{(2)}$ and $b_n^{(2)}$ have the following form

$$a_n^{(2)} = \frac{h_n^{(1)}(\rho_2)[\rho_2 j_n(\rho_2)]' - j_n(\rho_2)[\rho_2 h_n^{(1)}(\rho_2)]'}{h_n^{(1)}(\rho_1)[\rho_2 j_n(\rho_2)]' - \frac{\mu_2}{\mu_1} j_n(\rho_2)[\rho_1 h_n^{(1)}(\rho_1)]'}, \quad (1.20)$$

$$b_n^{(2)} = \frac{h_n^{(1)}(\rho_2)[\rho_2 j_n(\rho_2)]' - j_n(\rho_2)[\rho_2 h_n^{(1)}(\rho_2)]'}{\frac{\mu_2}{\mu_1} \frac{k_1}{k_2} h_n^{(1)}(\rho_1)[\rho_2 j_n(\rho_2)]' - \frac{k_2}{k_1} j_n(\rho_2)[\rho_1 h_n^{(1)}(\rho_1)]'}. \quad (1.21)$$

The coefficients $a_n^{(2)}$ and $b_n^{(2)}$ in the expansion of the Green function in vector spherical harmonics (eq. 1.19) have the same denominator as the coefficients c_n and d_n in the expansion of the field inside nanoparticle (eq. 1.8), that is, they have resonances at the same frequencies.

1.5 Non-linear materials: BaTiO₃, GaAs

The nanoparticles studied in this work will be assumed to be single-crystal, and we will denote the coordinate system x_c, y_c, z_c attached to the crystalline lattice.

The nonlinear susceptibility tensor $\chi_{ijk}^{(2)}$ responsible for the process of second harmonic generation and spontaneous parametric down-conversion. For a barium titanate BaTiO₃ particle, Figure 1.4(b), the

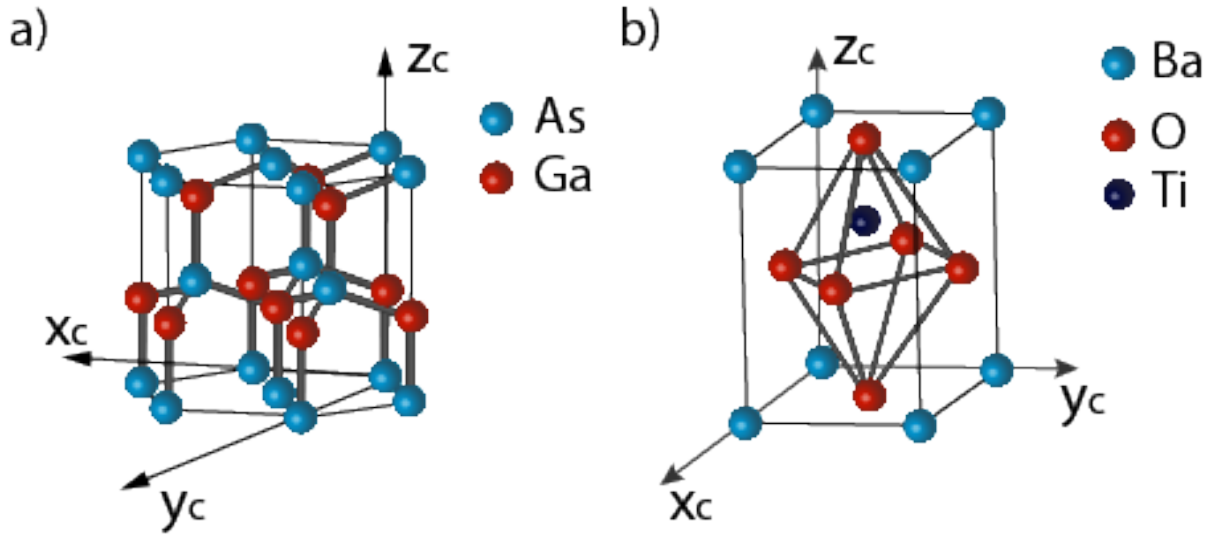


Figure 1.4 — (a) Gallium arsenide GaAs wurzite type crystal lattice with C_{6v} symmetry.(b) Barium titanate BaTiO₃ crystal lattice at room temperature with C_{4v} symmetry

refractive index in the optical range is $n \sim 2.4$, and $\chi_{ijk}^{(2)}$ is as follows [52]:

$$\chi_{ijx}^{(2)} = \begin{pmatrix} 0 & 0 & d_{15} \\ 0 & 0 & 0 \\ d_{31} & 0 & 0 \end{pmatrix}, \chi_{ijy}^{(2)} = \begin{pmatrix} 0 & 0 & 0 \\ 0 & 0 & d_{15} \\ 0 & d_{31} & 0 \end{pmatrix}, \chi_{ijz}^{(2)} = \begin{pmatrix} d_{15} & 0 & 0 \\ 0 & d_{15} & 0 \\ 0 & 0 & d_{33} \end{pmatrix}, \quad (1.22)$$

where $d_{15} = 17$ pm/V, $d_{31} = 15.7$ pm/V, $d_{33} = 6.8$ pm/V.

For a particle from wurzite type gallium arsenide GaAs , Figure 1.4(a), the refractive index in the optical range is $n \sim 3.6$, and $\chi_{ijk}^{(2)}$ as follows [53] has the same form as (eq. 1.22), but $d_{15} = 42$ pm/V, $d_{31} = 21$ pm/V and $d_{33} = 115$ pm/V. Next, we will consider the crystalline lattice rotated to $\beta = \pi/2$ around the y-axis, for this configuration the tensor will have the form

$$\chi_{ijx}^{(2)} = - \begin{pmatrix} d_{33} & 0 & 0 \\ 0 & d_{15} & 0 \\ 0 & 0 & d_{15} \end{pmatrix}, \chi_{ijy}^{(2)} = - \begin{pmatrix} 0 & d_{31} & 0 \\ d_{15} & 0 & 0 \\ 0 & 0 & 0 \end{pmatrix}, \chi_{ijz}^{(2)} = - \begin{pmatrix} 0 & 0 & d_{31} \\ 0 & 0 & 0 \\ d_{15} & 0 & 0 \end{pmatrix}. \quad (1.23)$$

Let us describe in more detail how we rotated the crystalline lattice, in subsequent sections we will have 3 rotations: rotation at angle γ around the z-axis, rotation at angle β around the y-axis and rotation at angle

α around the x-axis. The matrices of such rotations $R_x(\alpha)$, $R_y(\beta)$ and $R_z(\gamma)$ have the form

$$R_x(\alpha) = \begin{pmatrix} 1 & 0 & 0 \\ 0 & \cos(\alpha) & -\sin(\alpha) \\ 0 & \sin(\alpha) & \cos(\alpha) \end{pmatrix}, R_y(\beta) = \begin{pmatrix} \cos(\beta) & 0 & \sin(\beta) \\ 0 & 1 & 0 \\ -\sin(\beta) & 0 & \cos(\beta) \end{pmatrix},$$

$$R_z(\gamma) = \begin{pmatrix} \cos(\gamma) & -\sin(\gamma) & 0 \\ \sin(\gamma) & \cos(\gamma) & 0 \\ 0 & 0 & 1 \end{pmatrix}.$$

2 SPONTANEOUS PARAMETRIC DOWN- CONVERSION BY DIELECTRIC NANOPARTICLE

In present section we theoretical study spontaneous parametric down-conversion by spherical nanoparticle made of a nonlinear material with bulk nonlinearity tensor $\chi^{(2)}$ in the classical Mie geometry (Figure 1.2). We considered wurzite type gallium arsenide GaAs nanoparticle with radius of the sphere $a = 110$ nm. The nanoparticle is excited by a plane wave propagating along z -axis and polarized along x -axis. In this Section, spatial and polarization correlations between the generated photons are studied. In particular, the orientation of the emitted photons was studied and the general condition of the nonlinear analogue of the Kerker effect was obtained.

2.1 Linear Kerker effect

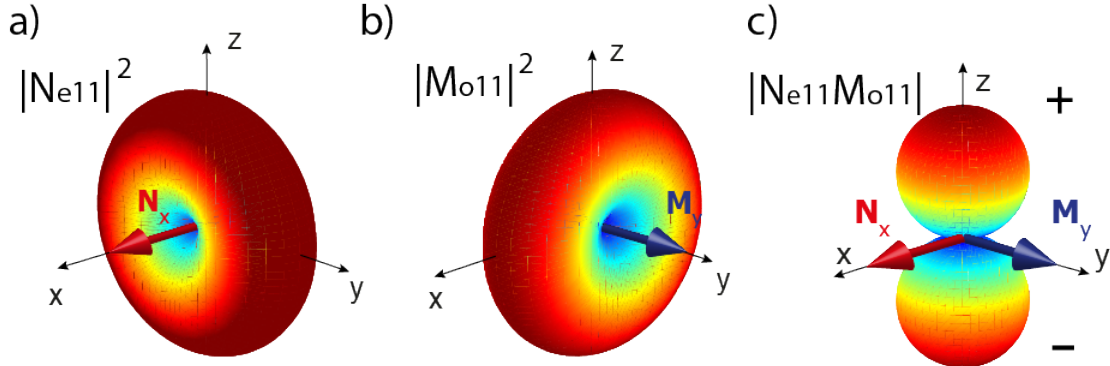


Figure 2.1 — Far field diagrams of radiation of electric dipole along x -axis (a), magnetic dipole along y -axis (b) and their composition (c), where the sign shows, they enter the electric field in phase (+) or in antiphase (-)

Before considering nonlinear generation, we start with an interpretation of the elastic Kerker effect in terms of the Mie modes.

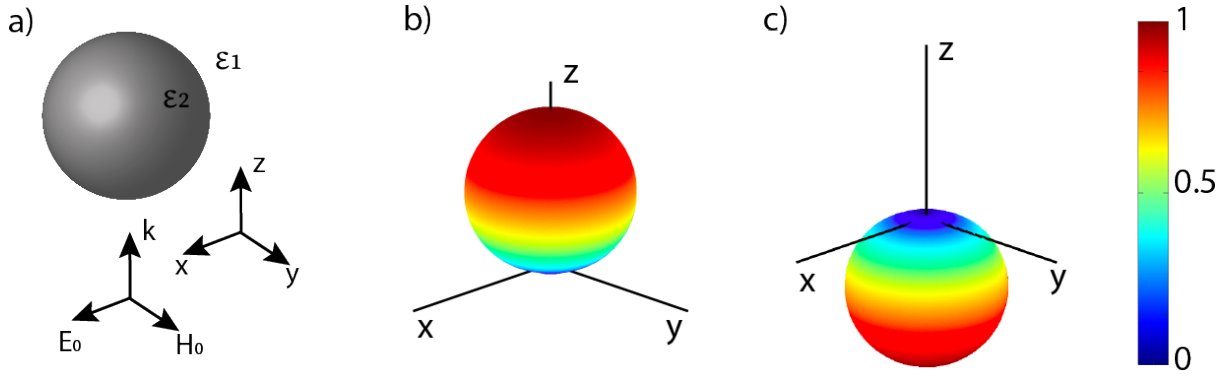


Figure 2.2 — (a) Configuration of the system. (b,c) Illustration of strong forward (b) and backward (d) scattering

In present Section 2 we consider only dipole modes with $n = 1$, so we can simplify notations in vector spherical harmonics (eq. 1.4-1.7) to $e_{11} = x$, $o_{11} = y$, $e_{01} = z$ in the expression for the scattered field \mathbf{E}_s (eq. 1.11). The Kerker effect can be interpreted in terms of the field structure and symmetry of these modes [54]. In the simplest case, directional light scattering arises due to the crossed magnetic dipole and electric dipole which contribute to the field with the different phases. In the dipolar approximation, the far-field Poynting vector of the scattered electromagnetic field describes the diagram of the elastic scattering. (For detailed derivation of equation 2.1, see Appendix A)

$$\begin{aligned}
|\mathbf{S}| \simeq & |E_1|^2 \left[|a_1|^2 |\mathbf{N}_x^{(1)}|^2 + |b_1|^2 |\mathbf{M}_y^{(1)}|^2 - \right. \\
& - 2|a_1^* b_1 \mathbf{N}_x^{(1)*} \mathbf{M}_y^{(1)}| \cos(\varphi_{b_1} - \varphi_{a_1}) \sin(\varphi_{M_y} - \varphi_{N_x}) - \\
& \left. - 2|a_1^* b_1 \mathbf{N}_x^{(1)*} \mathbf{M}_y^{(1)}| \cos(\varphi_{M_y} - \varphi_{N_x}) \sin(\varphi_{b_1} - \varphi_{a_1}) \right] \quad (2.1)
\end{aligned}$$

Here $\varphi_{a_1}, \varphi_{b_1}, \varphi_{M_y}$, and φ_{N_x} define correspondingly the phase of the complex valued a_1, b_1 coefficients and $\mathbf{N}_x^{(1)}, \mathbf{M}_y^{(1)}$ vector harmonics. In the Figure 2.2 diagrams are shown for the various terms in the expression 2.1. One can see that the last terms depend on both relative phases of: 1) electric and magnetic dipole amplitudes a_1 and b_1 and 2) corresponding vector harmonics $\mathbf{M}_y^{(1)}$ and $\mathbf{N}_x^{(1)}$. The latter contribution in the far-field domain $kr \gg 1$ provides that $\varphi_{M_y} - \varphi_{N_x} = -\pi/2$ for $\theta = 0$, while $\varphi_{M_y} - \varphi_{N_x} = \pi/2$ for $\theta = \pi$. Moreover, the amplitudes of the $\mathbf{M}_y^{(1)}$ and $\mathbf{N}_x^{(1)}$ harmonics at points $\theta = 0, \pi$ are equal due to the symmetry

of magnetic and electric dipole emission and using $|\mathbf{N}_x^{(1)}|^2 = |\mathbf{M}_y^{(1)}|^2 = |\mathbf{N}_x^{(1)*} \mathbf{M}_y^{(1)}|$, we come to a simple expression:

$$S(\theta = 0, \pi) \sim |E_1|^2 [|a_1|^2 + |b_1|^2 \pm 2|a_1^* b_1| \cos(\varphi_{b_1} - \varphi_{a_1})]$$

Basing on obtained expression, one comes to a well-known Kerker condition for strong forward scattering $|a_1| = |b_1|$ and $\varphi_{a_1} = \varphi_{b_1}$, Figure 2.2(a), or for strong backward scattering (second-Kerker's condition) $|a_1| = |b_1|$ and $\varphi_{b_1} - \varphi_{a_1} = \pi$, Figure 2.2(b). These simple results lie in the basis of directionality engineering with resonant dielectric structures.

2.2 Non-linear generation of entangled photons

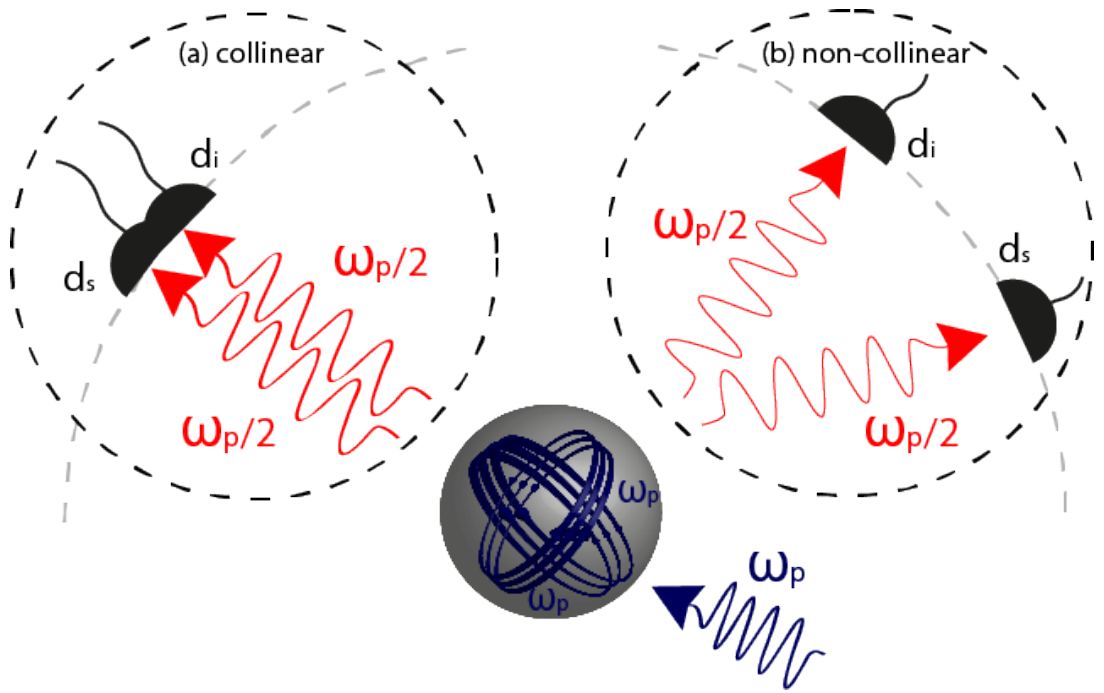


Figure 2.3 — Schematic of SPDC process. (a) Collinear decay: signal and idler photons decay in same direction $\mathbf{r}_i = \mathbf{r}_s$. (b) Non-collinear decay: signal and idler photons decay in different directions, but $|\mathbf{r}_i| = |\mathbf{r}_s|$

Within the SPDC process a two-photon states is generated through a nonlinear decay of a pump photon inside the nanoparticle. This process will be mediated by the resonant properties of the nanoparticle and can be described with a two-photon amplitude $T_{is}(\mathbf{r}_i, \omega_i, \mathbf{d}_i, \mathbf{r}_s, \omega_s, \mathbf{d}_s)$ equation 1.1,

expressing the probability of simultaneous detection of idler and signal photons having correspondingly frequencies ω_i and ω_s at coordinates \mathbf{r}_i and \mathbf{r}_s with polarization defined by the polarization of the detector \mathbf{d}_i and \mathbf{d}_s . Then, the probability of simultaneous detection of idler and signal photons of particular polarizations provided by the direction of \mathbf{d}_i and \mathbf{d}_s will be as follows

$$w_{\mathbf{d}_i, \mathbf{d}_s} = \frac{2\pi}{\hbar} \delta(\hbar\omega_i + \hbar\omega_s - \hbar\omega_p) |T_{is}|^2. \quad (2.2)$$

In the following, we will focus mainly on unpolarized detection, and the amplitude can be obtained by the direct summation of 2.2 over all possible polarizations of detectors: $w^{unpol} = \sum_{\mathbf{d}_i, \mathbf{d}_s} w_{\mathbf{d}_i, \mathbf{d}_s}$. We will also discuss the polarized entanglement in Section 2.4 for particular orientations of the detectors.

Next, we will provide the grounds for multipolar photon entanglement of the generated photons. In the case of nonlinear decay in bulk medium, there is a particular spatial and polarization correlation between the free-space photons described by plane waves. In the case of subwavelength scale nonlinear source, for which plane wave description is substituted by multipolar harmonics there can appear particular entanglement and correlations between the multipolar content of the generated photons. In order to analyze that, we expand the two-photon amplitude into particular multipolar channels. This can be done straight forwardly by expanding the Green's function (equation 1.19).

We will introduce additional notation to make the description of the considered process more compact and elegant. First of all, we will refer to vector spherical harmonics as $\mathbf{W}_{p_i p_r m n}(k, \mathbf{r})$ notation, where m and n are azimuthal and main quantum numbers, p_i and p_r are the inversion and reflection in plane $y = 0$ parities indexes. We will define the set of four labels as $\mathbf{J} = \{p_i, p_r, m, n\}$. Thus, the nonlinear decay process can be understood as a set of multipolar decay channels each characterized by \mathbf{J} -vectors

$\mathbf{J}_{pump} \rightarrow \mathbf{J}_{idler}, \mathbf{J}_{signal}$. The two-photon amplitude then can be expand as

follows:

$$\begin{aligned}
T_{is}(\mathbf{r}_i, \omega_i, \mathbf{d}_i; \mathbf{r}_s, \omega_s, \mathbf{d}_s) &= \sum_{\mathbf{J}_p, \mathbf{J}_i, \mathbf{J}_s} \tilde{T}_{\mathbf{J}_p \rightarrow \mathbf{J}_i, \mathbf{J}_s} \times \\
&\times D_{\mathbf{J}_p \rightarrow \mathbf{J}_i, \mathbf{J}_s} \left(\mathbf{d}_i^* \cdot \mathbf{W}_{\mathbf{J}_i}^{(1)}(k_{i1}, \mathbf{r}_i) \right) \left(\mathbf{W}_{\mathbf{J}_s}^{(1)}(k_{s1}, \mathbf{r}_s) \cdot \mathbf{d}_s^* \right)
\end{aligned} \tag{2.3}$$

where index 1 mean outside nanoparticle and, hence, we use $k_{1i,1s} = \sqrt{\varepsilon_1} \omega_{i,s} / c$, index 2 mean inside nanoparticle, hence, we use $k_{2i,2s} = \sqrt{\varepsilon_2(\omega_{i,s})} \omega_{i,s} / c$ and

$$\begin{aligned}
\tilde{T}_{\mathbf{J}_p \rightarrow \mathbf{J}_i, \mathbf{J}_s} &= - \left(\frac{\omega_i \omega_s}{c^2} \right)^2 k_{i2} k_{s2} A_{\mathbf{J}_i} A_{\mathbf{J}_s} B_{\mathbf{J}_p}, \\
A_{\mathbf{J}} &= (2 - \delta_0) \frac{2n + 1}{n(n + 1)} \frac{(n - m)!}{(n + m)!} \cdot \begin{cases} a_n^{(2)}, & \text{if } t = M \\ b_n^{(2)}, & \text{if } t = E \end{cases}, \\
B_{\mathbf{J}} &= E_n \cdot \begin{cases} c_n, & \text{if } t = M \\ -id_n, & \text{if } t = E \end{cases}.
\end{aligned}$$

Coefficients describing decaying channels contain harmonic from the pump field and two harmonics from dyadic green functions

$$D_{\mathbf{J}_p \rightarrow \mathbf{J}_i, \mathbf{J}_s} = \sum_{\alpha, \beta, \gamma} \chi_{\alpha\beta\gamma} \int_V W_{\mathbf{J}_p, \gamma}(k_2, \mathbf{r}_0) W_{\mathbf{J}_i, \alpha}(k_{i2}, \mathbf{r}_0) W_{\mathbf{J}_s, \beta}(k_{s2}, \mathbf{r}_0) d^3 r_0, \tag{2.4}$$

where $W_{\mathbf{J}, \alpha}(k, \mathbf{r})$ is the Cartesian projection of the vector spherical harmonic on α -axis. The D-coefficients (eq. 2.4) are the overlapping integral and determine the amplitude of particular decay channel and equal to zero for a large number them. The non-zero values of D-coefficients provide allowed transitions and define the so-called selection rules of second order nonlinear process. The detailed symmetry based analysis is provided elsewhere [55] for the inverse process of sum frequency generation. Below we will discuss in more details what particular decay channels can contribute into the directional emission of entangled photons.

The rate of simultaneous detection can be obtained directly from equation 2.3. Our task is to find the conditions, which will provide directional emission of the correlated photons. On this way, we in the first

row will focus on total coincidence rate w^{unpol} , which does not resolve the polarization state of the generated photons.

$$\begin{aligned}
w_{i_s}^{unpol}(\mathbf{r}_i, \omega_i; \mathbf{r}_s, \omega_s) &\sim \sum_{\mathbf{d}_i, \mathbf{d}_s} |T_{i_s}(\mathbf{r}_i, \omega_i, \mathbf{d}_i; \mathbf{r}_s, \omega_s, \mathbf{d}_s)|^2 \\
&\sim \sum_{\mathbf{d}_i, \mathbf{d}_s} \sum_{\substack{\mathbf{J}_p, \mathbf{J}_i, \mathbf{J}_s \\ \mathbf{J}'_p, \mathbf{J}'_i, \mathbf{J}'_s}} \underbrace{\tilde{T}_{\mathbf{J}_p \rightarrow \mathbf{J}_i, \mathbf{J}_s} \cdot D_{\mathbf{J}_p \rightarrow \mathbf{J}_i, \mathbf{J}_s} \cdot \tilde{T}_{\mathbf{J}'_p \rightarrow \mathbf{J}'_i, \mathbf{J}'_s}^* \cdot D_{\mathbf{J}'_p \rightarrow \mathbf{J}'_i, \mathbf{J}'_s}^*}_{C_{\mathbf{J}'_p \rightarrow \mathbf{J}'_i, \mathbf{J}'_s}^{\mathbf{J}_p \rightarrow \mathbf{J}_i, \mathbf{J}_s}} \times \left(\mathbf{d}_i^* \cdot \mathbf{W}_{\mathbf{J}_i}^{(1)}(k_{i1}, \mathbf{r}_i) \right) \times \\
&\quad \times \left(\mathbf{W}_{\mathbf{J}_s}^{(1)}(k_{s1}, \mathbf{r}_s) \cdot \mathbf{d}_s^* \right) \times \left(\mathbf{d}_i \cdot \mathbf{W}_{\mathbf{J}'_i}^{*(1)}(k_{i1}, \mathbf{r}_i) \right) \left(\mathbf{W}_{\mathbf{J}'_s}^{*(1)}(k_{s1}, \mathbf{r}_s) \cdot \mathbf{d}_s \right) \\
&\sim \sum_{\substack{\mathbf{J}_p, \mathbf{J}_i, \mathbf{J}_s \\ \mathbf{J}'_p, \mathbf{J}'_i, \mathbf{J}'_s}} C_{\mathbf{J}'_p \rightarrow \mathbf{J}'_i, \mathbf{J}'_s}^{\mathbf{J}_p \rightarrow \mathbf{J}_i, \mathbf{J}_s} \left(\mathbf{W}_{\mathbf{J}_i}^{(1)}(k_{i1}, \mathbf{r}_i) \cdot \mathbf{W}_{\mathbf{J}'_i}^{*(1)}(k_{i1}, \mathbf{r}_i) \right) \left(\mathbf{W}_{\mathbf{J}_s}^{(1)}(k_{s1}, \mathbf{r}_s) \cdot \mathbf{W}_{\mathbf{J}'_s}^{*(1)}(k_{s1}, \mathbf{r}_s) \right)
\end{aligned} \tag{2.5}$$

The obtained expression can be considered as an analogue of expression 2.1 but for nonlinear generation of the correlated photons. Each component in the sum consists of the multiplication of two idler photons (\mathbf{J}_i and \mathbf{J}'_i) and two signal photons (\mathbf{J}_s and \mathbf{J}'_s) as all of them can potentially interfere due to coherence of the SPDC process. Among the variety of the detection geometries, we will specify a *collinear* detection, when the idler and signal detectors are located in the same point $\mathbf{r}_i = \mathbf{r}_s$ and *non-collinear* detection, when photons decay in different directions, but $|\mathbf{r}_i| = |\mathbf{r}_s|$ (See Figure 2.3).

2.3 Directional emission from GaAs nanoparticle

We apply the theoretical background overview in the previous section to analyzing the nonlinear generation of correlated photons from a nanoparticle made of a material with strong bulk nonlinearity such as GaAs gallium arsenide, III-V semiconductor materials have already been widely used for second-harmonic generation in a number of experiments [53, 56] showing particular enhancement of nonlinear signal generation owing to pronounced Mie resonance in the visible and infrared region. Indeed, the elastic scattering spectrum of a spherical particle of radius $a = 110$ nm is shown in Figure 2.4(a) For the given sizes the nanoparticle

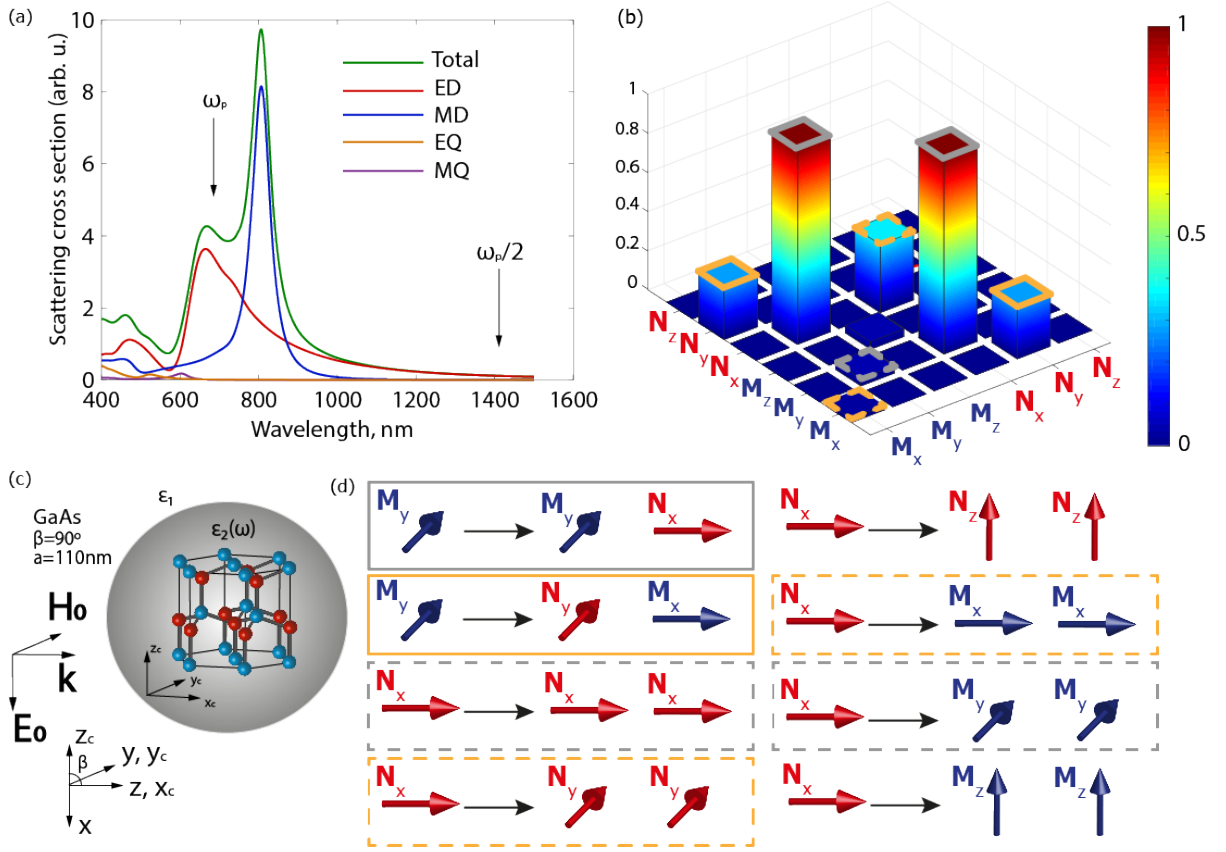


Figure 2.4 — (a) Scattering cross-section including different multipoles (green - total, red- electric dipole ED, blue-magnetic dipole MD ,orange- electric quadrupole EQ , purple- magnetic quadrupole MQ) (b,d) Possible decay channels in considering geometry at $\lambda_p = 720$ nm, grey or yellow needed to directivity: solid - decay to the crossed dipoles, dashed - decay to the same dipoles (c) Geometry of the considered problem. Spherical particle of wurtzite GaAs with a radius $a = 110$ nm, rotated to the $\beta = 90^\circ$ around y axis

demonstrate electric (ED) and magnetic (MD) dipole resonances. Their interference results in directional (elastic) scattering of in accordance to Kerker effect overviewed in Section 2.1. In this Section 2.3, we apply several limitation, which on one hand will simplify the model, and on the other will provide all the insight of the directional emission of correlated photons:

- 1) we focus on resonant pumping scheme, when the the frequency of the exciting field matches the electric and magnetic dipole resonances;

2) we consider degenerate process assuming $\omega_i = \omega_s = \omega_p/2$, thus the generated photons will be far from the Mie resonance in the long-wavelength region;

3) we neglect the birefringence of GaAs material, which does not provide strong contribution to second-order nonlinear process;

4) for the sake of definiteness, we will be interested in the strong directivity in forward/backward directions of collinear emission of correlated photons, i.e. along z -axis. (This one provides a more clear and simple narrative at this stage, however will be generalized in the following.)

The nonlinear response of GaAs is defined predominantly by the structure of its nonlinear tensor $\chi^{(2)}$ which was described in detail in Section 1.5. The particular form of the tensor dictates the selection rules of the SPDC process through the non-zero D -coefficients expression 2.4. For the proposed form of the nonlinear tensor, the non-zero dipole decay channels are summarized in Figure 2.4(b,d) under the assumption that the pumping field generates the x -oriented ED and y -oriented MD modes. These channels define the non-zero components in the coincidence rate w^{unpol} expression 2.5, while the scalar products of the vector functions corresponded to these modes, define the far-field pattern of $w^{unpolar}$, which will be presented in the next Section 2.3.1.

2.3.1 Forward/backward directivity

As mentioned above, we are interested in z -directivity of collinear detection, Figure 2.3(a), i.e. when two correlated photons are generated either in forward or backward direction with respect to the direction of the exciting pump. In this formulation, this will provide us with a two-photon analogue of the Kerker effect. Thus, careful analysis of different contributions of scalar products in equation 2.5 schematically summarized in Figure A.1 shows that only a few components give contribution to the forward and backward directivity, which are scalar products $\mathbf{M}_y^{(1)} \cdot \mathbf{N}_x^{(1)}$ and $\mathbf{M}_x^{(1)} \cdot \mathbf{N}_y^{(1)}$. The bigger part of the components do not contribute

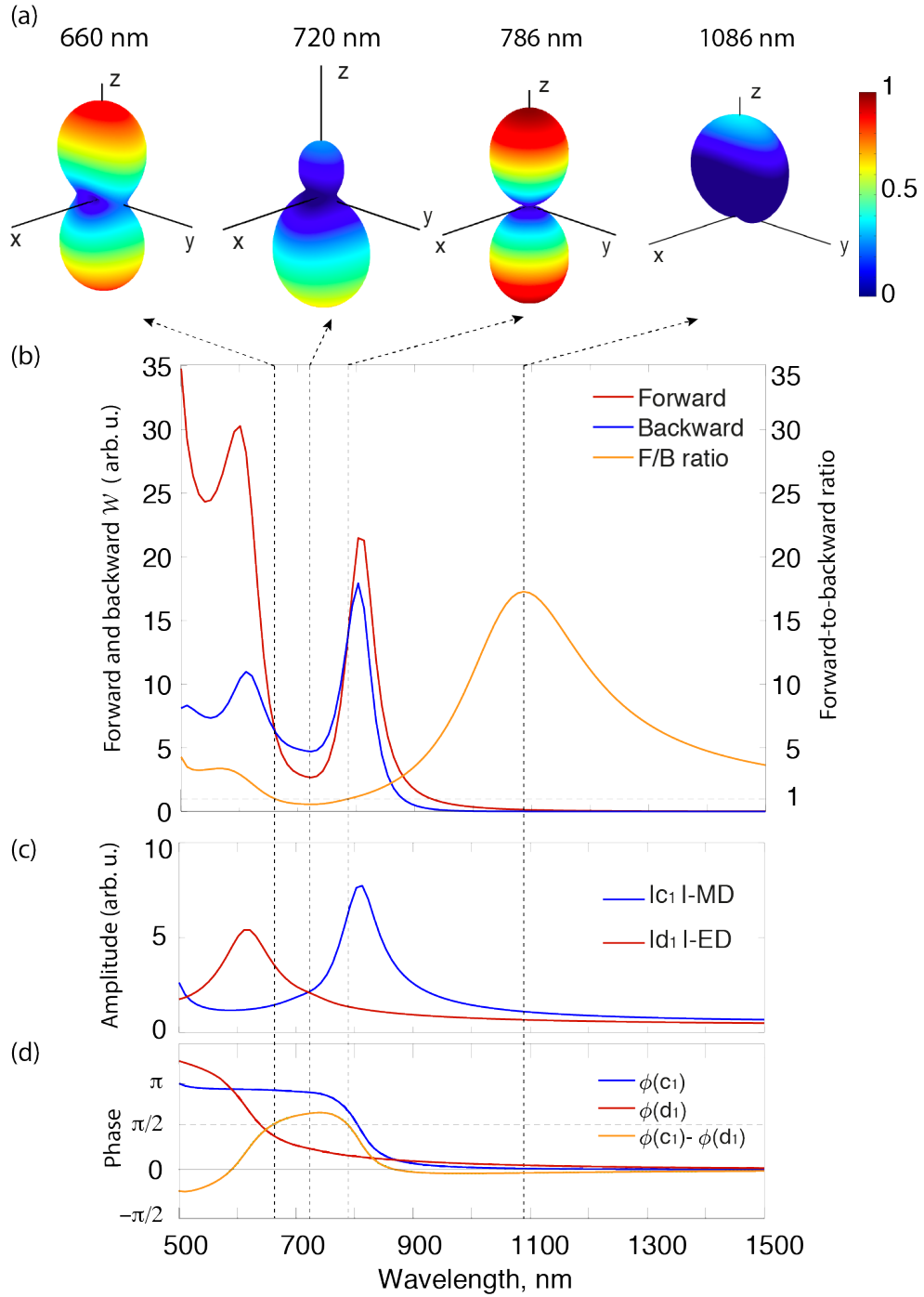


Figure 2.5 — (a) The far-field patterns of collinear two-photon generation for different wavelengths $\lambda_p = 660$ nm, 720 nm, 786 nm, 1086 nm. (b) Forward and backward w_{unpol} and their ratio depending on pump wavelength λ_p . (c) Amplitudes of coefficients $|c_1|$ and $|d_1|$ in decomposition of pump field inside nanoparticle \mathbf{E}_p . (d) Phases of this coefficients and their phase difference $\varphi_{c_1} - \varphi_{d_1}$

to the collinear coincidence rate in $\theta = 0, \pi$ directions, which significantly simplifies the analysis. Thus, to get the insights of the directional emission

of correlated, we derive an expression for the asymmetry of the detection rate $\Delta w^{unpol} = w_{\theta=0}^{unpol} - w_{\theta=\pi}^{unpol}$ is the proposed configuration. By taking into account that the decay of the photons is out of the resonance with the Mie modes (see Figure 2.4), it can be assumed that the phase difference between the ED and MD coefficients at the decay frequency $\omega_p/2$ is zero $\Delta\varphi^{decay} = \varphi_{a_1} - \varphi_{b_1} \approx 0$, as shown in Figure 2.5(d). Then the expression of the asymmetry can be expressed in a simple form (a little more about this in the Appendix A):

$$\Delta w^{unpol} \sim |a_1^{(2)} b_1^{(2)} c_1 d_1| \cos(\Delta\varphi^{pump}) \left[\alpha |a_1^{(2)}|^2 + \beta |b_1^{(2)}|^2 \right], \quad (2.6)$$

$$\alpha = D_{N_x \rightarrow M_x, M_x} D_{M_y \rightarrow M_x, N_y} - D_{N_x \rightarrow M_y, M_y} D_{M_y \rightarrow M_y, N_x},$$

$$\beta = D_{N_x \rightarrow N_x, N_x} D_{M_y \rightarrow N_x, M_y} - D_{N_x \rightarrow N_y, N_y} D_{M_y \rightarrow N_y, M_x},$$

where $a_1^{(2)}$ and $b_1^{(2)}$ are coefficients in Green function (eq. 1.19), that describes modes on which photons decay, c_1 and d_1 are coefficients in pump field (eq. 1.8) and $D_{J_p \rightarrow J_i, J_s}$ overlapping coefficient (eq. 2.4), which shows decay amplitude. The expression 2.6 provides a simple yet clear result on the origin of the two-photon generation directivity. First of all, one need to mention there is the factor responsible for elastic directivity containing in particular the phase difference between ED and MD modes at the fundamental frequency $\Delta\varphi^{pump} = \varphi_{c_1} - \varphi_{d_1}$. Thus, the directionality of the collinear two-photon detection can be expected for the same in-phase or out-of-phase conditions as common Kerker effect. Secondly, there is an additional factor in square brackets, which strongly differs two-photon generation from the elastic scattering case. It contains mode amplitudes a_1 and b_1 multiplied by α and β coefficients, which contain the amplitudes of the decay. For the cases shown in Figure 2.5 the factor in the square brackets in equation 2.6 is strictly positive, however it strongly depends on the particular modes involved in the decay process and can freely change its sign. The spectral dependence of α - and β -factors for the parameters used in Figure 2.5 is provided in Figure 2.6.

The directional generation of entangled photons is illustrated in Figure 2.5(a), where in block the directivity of collinear generation is shown for different pumping wavelengths λ_p . The spectrum of forward-

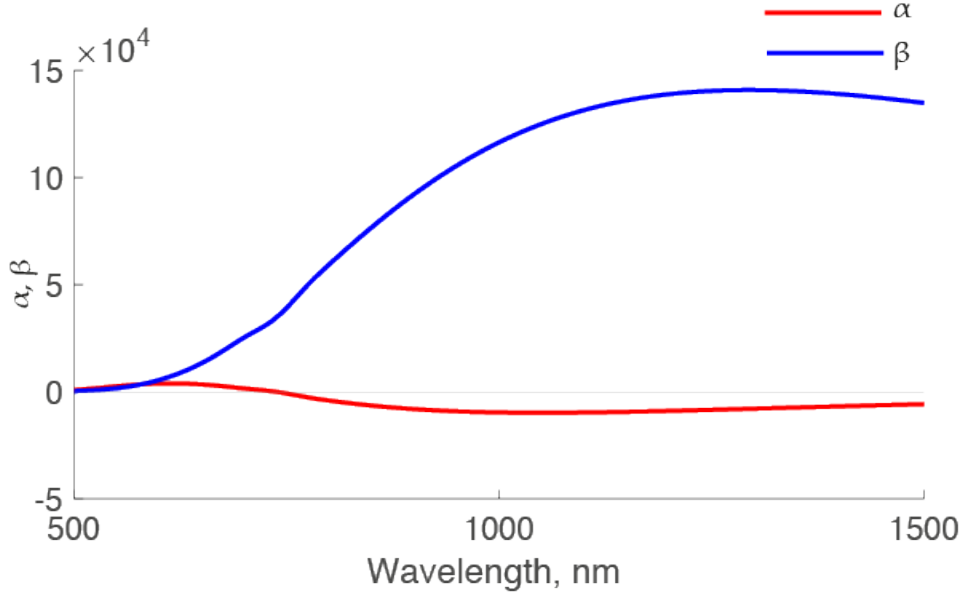


Figure 2.6 — Dependence of α and β coefficients in the equation 2.6 on the fundamental wavelength λ_p

to-backward ratio $w_{\theta=0}^{unpol}/w_{\theta=\pi}^{unpol}$ is shown in Figure 2.5(b) demonstrating strong backward two-photon scattering at $\lambda_p = 720$ nm and forward scattering at $\lambda_p = 1286$ nm. The corresponding amplitudes and phases of the Mie coefficients governing the nonlinear decay are shown in panels in Figure 2.5(b-c), which show that in the course of resonant collinear decay the Kerker-type conditions are applied for the pumping dipole modes providing directional photon generation.

When quadrupole terms are included in the pump field (eq. 1.8), but decay still occurs in the wavelength range, where only dipole components can be taken into account, the following generalization of the equation 2.6 can be obtained equation 2.7, where the second term shows the contribution from the interference of magnetic and electric quadrupoles in the pump field $\Delta\varphi_{EQMQ}^{pump} = \varphi_{c_2} - \varphi_{d_2}$, third term shows the contribution from the interference of magnetic dipole and magnetic quadrupole in the pump field $\Delta\varphi_{MDMQ}^{pump} = \varphi_{c_2} - \varphi_{c_1}$ and last term shows the contribution from the interference of electric dipole and electric quadrupole in the pump field $\Delta\varphi_{EDEQ}^{pump} = \varphi_{d_2} - \varphi_{d_1}$.

$$\begin{aligned}
\Delta w^{unpol} \sim & |a_1^{(2)} b_1^{(2)} c_1 d_1| \cos(\Delta\varphi^{pump}) \left[\alpha |a_1^{(2)}|^2 + \beta |b_1^{(2)}|^2 \right] + \\
& + |a_1^{(2)} b_1^{(2)} c_2 d_2| \cos(\Delta\varphi_{EQMQ}^{pump}) \left[\alpha_2 |a_1^{(2)}|^2 + \beta_2 |b_1^{(2)}|^2 \right] + \\
& + |a_1^{(2)} b_1^{(2)} c_1 c_2| \cos(\Delta\varphi_{MDMQ}^{pump}) \left[\alpha_{12} |a_1^{(2)}|^2 + \beta_{12} |b_1^{(2)}|^2 \right] + \\
& + |a_1^{(2)} b_1^{(2)} d_1 d_2| \cos(\Delta\varphi_{EDEQ}^{pump}) \left[\alpha_{21} |a_1^{(2)}|^2 + \beta_{21} |b_1^{(2)}|^2 \right], \tag{2.7}
\end{aligned}$$

where the coefficients α_2, β_2 in second term are as follows

$$\begin{aligned}
\alpha_2 &= D_{M_{o12} \rightarrow M_x, M_x} D_{N_{e12} \rightarrow M_x, N_y} - D_{M_{o12} \rightarrow M_y, M_y} D_{N_{e12} \rightarrow M_y, N_x}, \\
\beta_2 &= D_{M_{o12} \rightarrow N_x, N_x} D_{N_{e12} \rightarrow N_x, M_y} - D_{M_{o12} \rightarrow N_y, N_y} D_{N_{e12} \rightarrow N_y, M_x}.
\end{aligned}$$

The coefficients α_{12}, β_{12} in third term in equation 2.7 are as follows

$$\begin{aligned}
\alpha_{12} &= D_{M_{o12} \rightarrow M_x, M_x} D_{M_y \rightarrow M_x, N_y} - D_{M_{o12} \rightarrow M_y, M_y} D_{M_y \rightarrow M_y, N_x}, \\
\beta_{12} &= D_{M_{o12} \rightarrow N_x, N_x} D_{M_y \rightarrow N_x, M_y} - D_{M_{o12} \rightarrow N_y, N_y} D_{M_y \rightarrow N_y, M_x}.
\end{aligned}$$

The coefficients α_{21}, β_{21} in last term in equation 2.7 are as follows

$$\begin{aligned}
\alpha_{21} &= D_{N_x \rightarrow M_x, M_x} D_{N_{e12} \rightarrow M_x, N_y} - D_{N_x \rightarrow M_y, M_y} D_{N_{e12} \rightarrow M_y, N_x}, \\
\beta_{21} &= D_{N_x \rightarrow N_x, N_x} D_{N_{e12} \rightarrow N_x, M_y} - D_{N_x \rightarrow N_y, N_y} D_{N_{e12} \rightarrow N_y, M_x}.
\end{aligned}$$

Thus, the condition for directional generation, when we take quadrupoles into account in pump field (eq. 1.8) is a little more complicated, but has the same structure for additional terms as was shown in eq. 2.6.

2.3.2 Generalized directivity conditions

The directivity of the photon generation supposed in this Section is based on electric and magnetic dipoles interference. Thus, these modes should be allowed in decaying channels, which in their turn are defined by the crystalline structure of the material, and also one should expect to observe cross-polarized ED and MD generations. It turns out, that depending on the crystalline structure of the material one expect observing directivity of photon emission in arbitrary directions. Figure 2.7 summarizes different crystalline structures of nonlinear materials

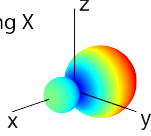
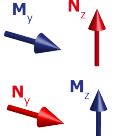
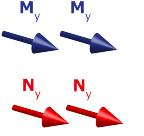
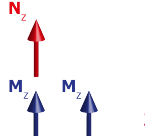
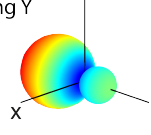
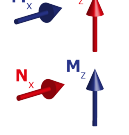
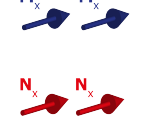
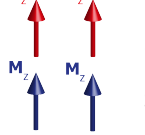
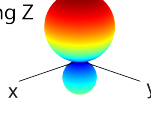
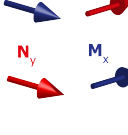
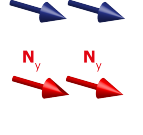
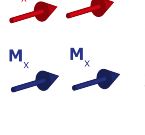
| Directivity | Decay on crossed dipoles | Decay on co-aligned dipoles | Non-zero $\chi^{(2)}$ components | Groups of symmetry |
|--|---|--|---|---|
| along X  |  |  Or  | xxx xyy xzz xyz xxz xyx yxx yyy yzz yyz yxz yxy zxx zyy zzz zyz zxz zxy | C_1 C_{1h} C_3 |
| along Y  |  |  Or  | xxx xyy xzz xyz xxz xyx yxx yyy yzz yyz yxz yxy zxx zyy zzz zyz zxz zxy | C_1 C_3 D_3 |
| along Z  |  |  Or  | xxx xyy xzz xyz xxz xyx yxx yyy yzz yyz yxz yxy zxx zyy zzz zyz zxz zxy | C_1 C_{1h} C_3 D_3 C_{3h} |

Figure 2.7 — Illustration of the necessary conditions for observing directivity along various axes. First column shows directionality, 2nd column shows first decay needed into two crossed magnetic and electric dipoles, 3rd column shows second decay needed into two similar dipoles.

The fourth column shows which tensor components of $\chi^{(2)}$ should be zero for the presence of the necessary decay channels. The last column shows symmetry groups, for which these components of the tensor are non-zero

which provides directional collinear generation of entangled photons and corresponding dipole channels of decay. One can see that depending on the orientation of crossed ED and MD the directivity of the photon emission can be preferable in x -, y -, or z -axis. One should stress that besides the crossed ED/MD terms the co-aligned dipole terms are also present but they do not contribute into directional emission.

2.4 Polarization correlations

In this Section we will consider the configuration of the system closer to the actual experiment, where the detectors collect the signal not at a specific point as at collinear decay $\mathbf{r} = \mathbf{r}_i = \mathbf{r}_s$, but in a certain area shown in the Figure 2.8(a), where the angle of maximum expansion regarding to the direction of maximum generation in collinear decay equal to $\theta = \frac{\pi}{3}$. Non-collinear decay shown in Figure 2.3(b) already

takes place in such geometry. Having fixed the wavelength of the incident

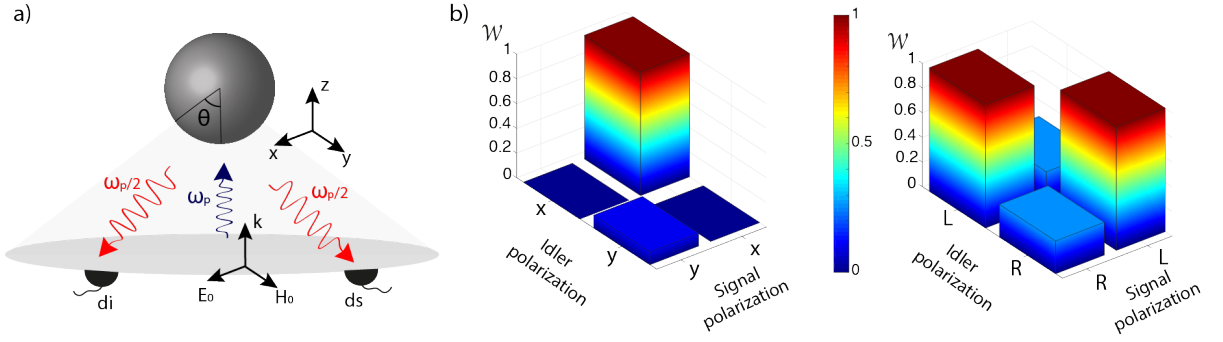


Figure 2.8 — (a) The configuration of the system under the study, the incident field propagating along z-axis and oscillates along x-axis.

Incident wavelength equal 720 nm and detection of signal and idler photons occurs in the area bounded by the angle of θ relative to the direction of the opposite z-axis. (b) Probability of detecting photons of various combinations in a linear basis including polarizations along x- and y- axis and in a circular basis including right circular (R) and left circular (L) polarizations

field $\lambda_p = 720 \text{ nm}$, we examined the polarization correlations between the emitted photons in two different bases — linear and circular. When considering in a linear basis, we have a situation in which, with the highest probability, polarization of the photons are equal and have the same polarization as the incident field along the x-axis $\mathbf{d}_{i(s)} = d_{i(s)}\mathbf{e}_x$, but this two-photon quantum state is not completely splittable, that is, the two-photon wave function $\varphi_{two\text{-photons}}$ cannot be represented as the product of the wave functions of the signal φ_{signal} and idler φ_{idler} photons $\varphi_{two\text{-photons}} \neq \varphi_{signal} \cdot \varphi_{idler}$. When considering in a circular basis with the highest probability photons polarizations are differ: one of the photons is right-circular polarized and the other left-circular polarized, thus, $\mathbf{d}_{i(s)} = d_{i(s)}/\sqrt{2}(\mathbf{e}_x \pm i\mathbf{e}_y)$. However, this state is not a pure Bell state [57].

3 SECOND HARMONIC GENERATION BY HYBRID METAL-DIELECTRIC NANOANTENNA

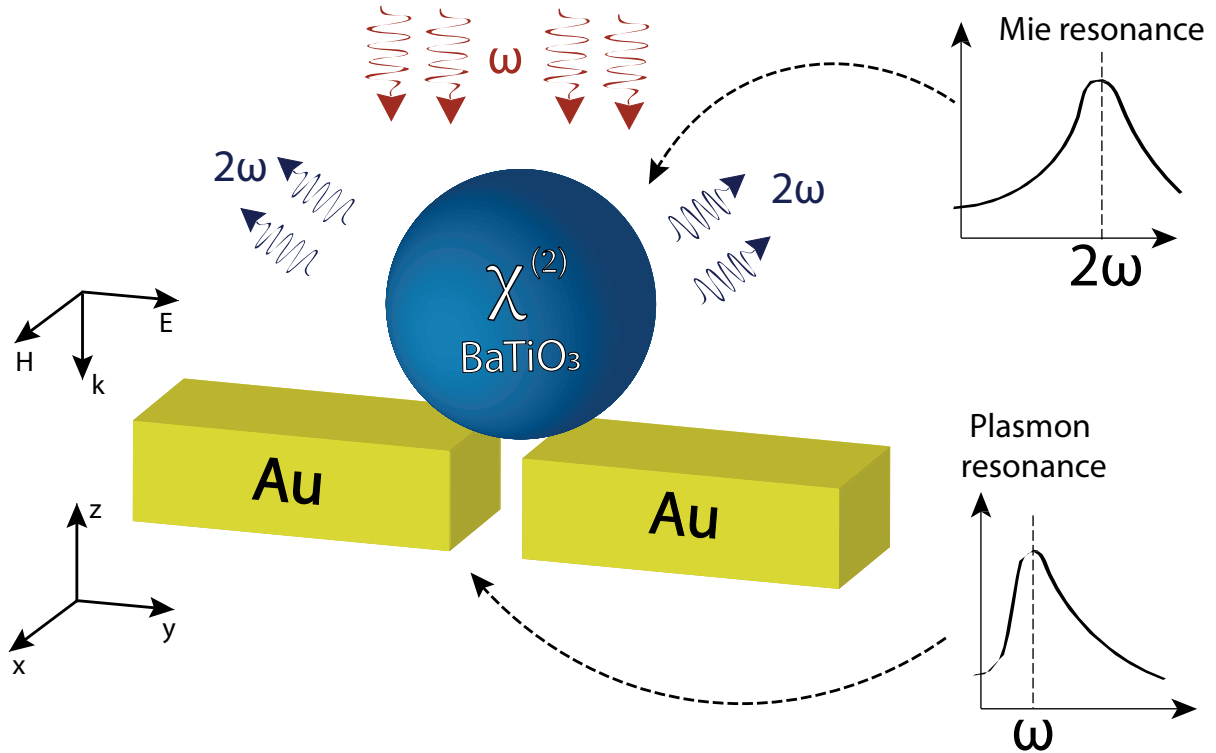


Figure 3.1 — Scheme of a bi-resonance hybrid nanoantenn. Plasmon resonance is fixed at the frequency of the incident field ω . Mie resonance is set at the the second harmonic generation frequency 2ω

In this Section, we theoretically propose and experimentally show a design of a dimer nanorod antenna made of gold and a monocrystalline BaTiO₃ nanosphere with two resonances tuned to the pump and SHG wavelength, respectively. Our goal is to use the first resonance to concentrate the energy of the incident light efficiently in the nonlinear material, and the second resonance is utilized to enhance the emission of the SHG [58, 59].

3.1 Analysis of the resonance properties of a hybrid nanoantenna

For definiteness, we fix the incident wavelength equal to 1000 nm, then the SHG will occur at 500 nm. We select the parameters of the hybrid antenna so that its plasmon resonance falls on the incident wavelength, and the Mie resonance on the SHG wavelength. To do this, we use the methods described in Sections 1.2, 1.3 and obtain the spectra of scattering efficiency on dielectric and plasmon systems. Then, changing the configuration of the systems, we will tune at the plasmon resonance and the Mie resonance at 1000 nm and 500 nm, respectively.

3.1.1 Scattering on a BaTiO₃ spherical nanoparticle

We use the results of Mie theory to find the scattering efficiency η_{scat} for spherical BaTiO₃ nanoparticle. By changing the radius of the nanoparticle r , we obtain that for $r = 95$ nm the magnetic dipole MD resonance will be at 500 nm, Figure 3.2(b).

Note that in the visible range, a nanoparticle with a radius $r = 95$ nm

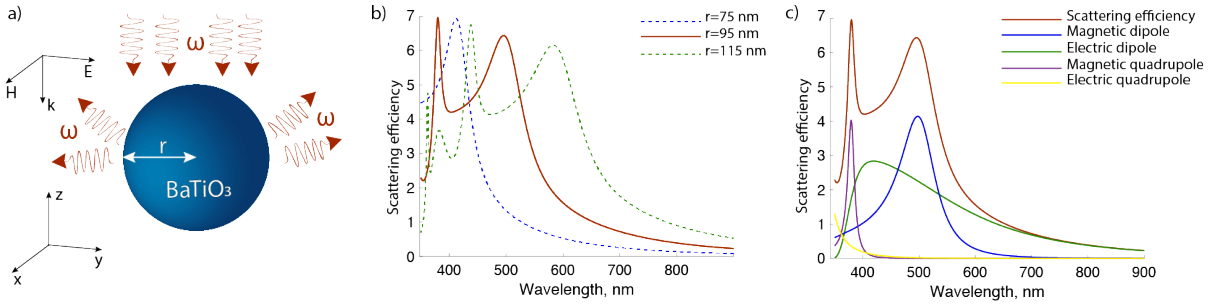


Figure 3.2 — (a) Scattering on a BaTiO₃ spherical nanoparticle in Mie configuration. (b) Spectral dependence of linear scattering efficiency η_{scat} for various radii of a spherical nanoparticle $r = 75$ nm, 95 nm, 115 nm. (c) The spectral dependence of the scattering efficiency η_{scat} on a BaTiO₃ with a radius $r = 95$ nm, the contributions of various multipoles are shown in color: red — total, green — electric dipole (ED), blue — magnetic dipole (MD), yellow — electric quadrupole (EQ) and purple is the magnetic quadrupole (MQ)

also has two more resonances: electric dipole ED shown in green, and

magnetic quadrupole MQ shown in blue in Figure 3.2(c), located at shorter wavelengths.

3.1.2 Scattering on a gold nanodimer

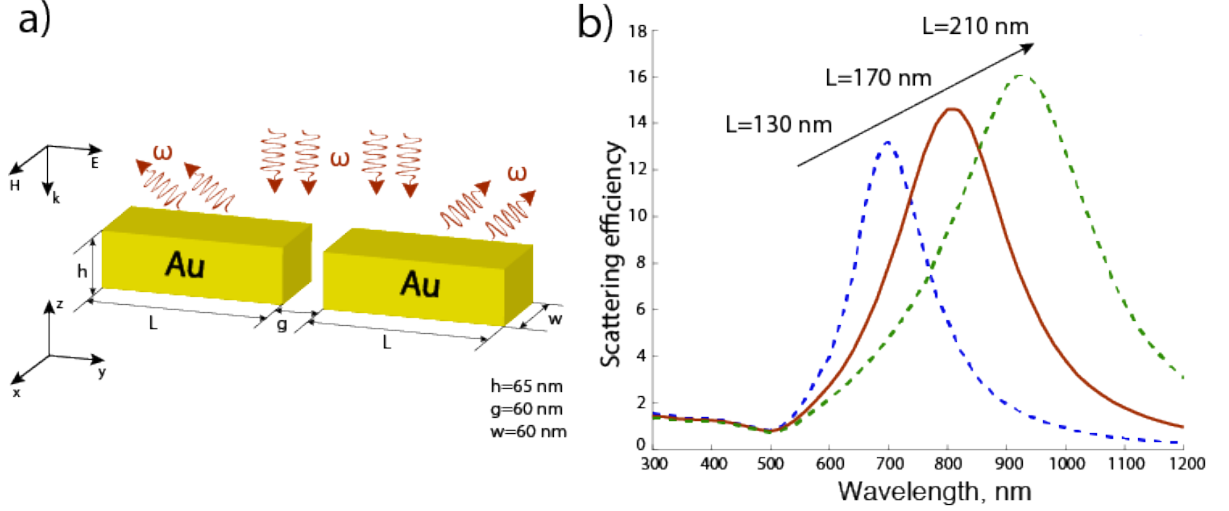


Figure 3.3 — a) Scattering on a plasmonic dimer nanoantenna made with Au. (b) Spectral dependence of the scattering efficiency η_{scat} for various lengths of golden bars $L = 130$ nm, 170 nm, 210 nm. For fixed dimensions in the x - z plane ($h = 65$ nm, $w = 60$ nm) and a fixed gap between the bars $g = 60$ nm

Using the package Comsol Multiphysics, we solve the problem of scattering on gold nanoantennas at wavelengths from 300 nm to 1200 nm with step of 10 nm. The optical parameters for Au were taken from Ref. [60]. The position of the plasmon resonance depends on the gap between the particles: the narrower the gap, the stronger the interaction between the plasmon modes of the individual nanoantennas, and hence the greater the splitting of the resonances. It is also known that the position of the plasmon resonance of elongated metal particles (not necessarily rectangles) depends on their length: the longer the particle, the stronger the resonance is shifted to the long-wavelength region [61]. We fix the cross section of the nanoantennas with a height $h = 65$ nm and a width $w = 60$ nm. We choose a gap width $g = 60$ nm and change the length of the gold particles L until the plasmon resonance reaches 1000 nm. As result, we get that a suitable length $L = 210$ nm. In addition

to the dipole resonance at 980 nm, the obtained nanoantenna has another weakly pronounced resonance at 400 nm, which corresponds to the second dipole mode.

The field inside the gap between the nanorods, for parameters $g = 20$ nm

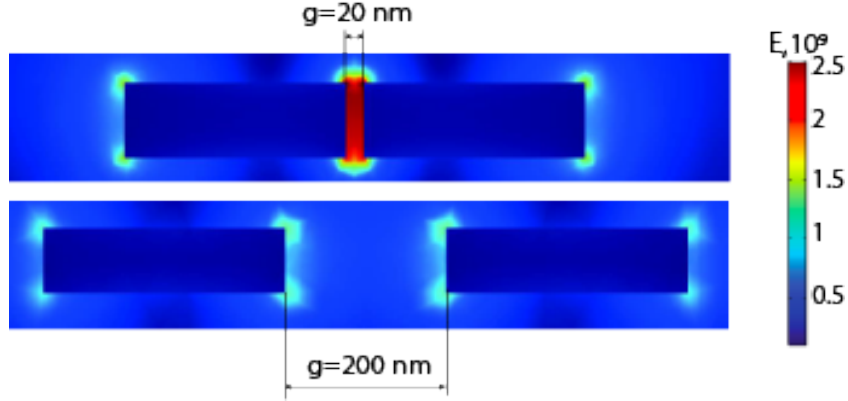


Figure 3.4 — Distribution of norm of electric field for gap $g = 20$ nm and $g = 200$ nm in the y - z plane.

and $g = 60$ nm, will be significantly enhanced comparing to a separate gold nanoantenna due to a hotspot[62]. To verify this, in the Comsol Multiphysics we plotted the field distribution near the nanoantenna at $g = 20$ nm, and compare it with the case, when there is no interaction between the modes of individual particles, for example, $g = 200$ nm, as shown in Figure 3.4.

3.1.3 Scattering on a hybrid bi-resonance nanoantenna

We study the linear optical properties of the hybrid Au-BaTiO₃ nanoantenna and compare them with the properties of individual plasmon and dielectric components. Based on the parameters obtained in previous Sections (3.1.1, 3.1.2), several nanoantennas were considered. In this and subsequent Sections, modeling on real sizes will be presented, namely, radius of the BaTiO₃ sphere $r \sim 96$ nm, length of the nanorods arms $L = 170$ nm, their height $h = 65$ nm, width $w = 60$ nm and gap between Au nanorods $g = 60$ nm. We consider scattering on a hybrid system with these parameters on a glass substrate with the refractive index $n = 1.5$, Figure 3.5(a), and we get the spectrum of scattering

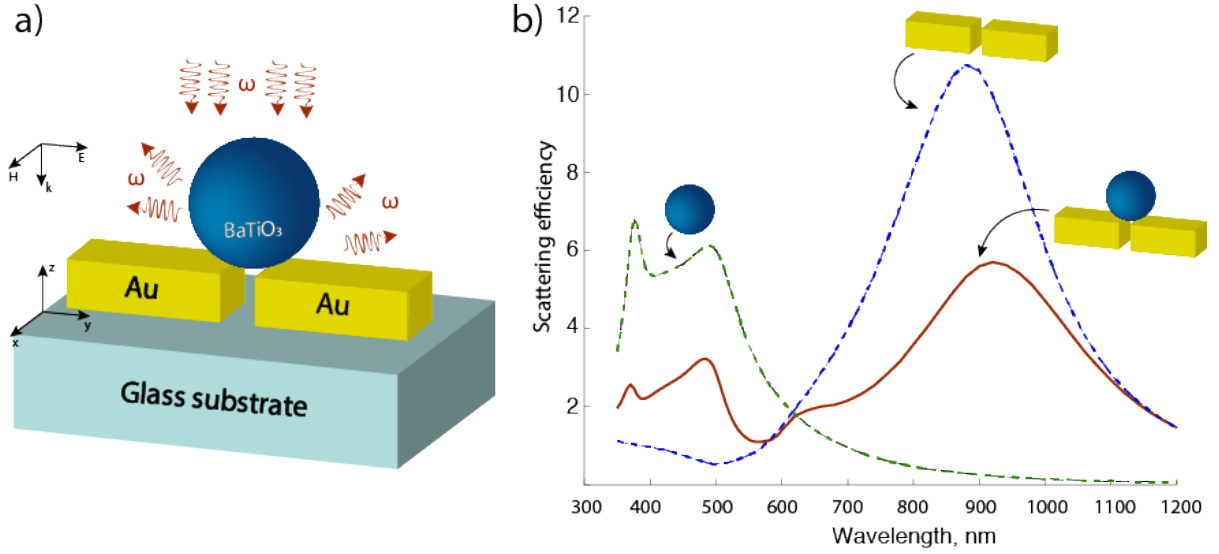


Figure 3.5 — (a) Scattering by a bi-resonant hybrid nanoantenna. (b)

Spectral dependence of the scattering efficiency η_{scat} for a hybrid Au-BaTiO₃ nanoantenna on a glass substrate with a refractive index $n = 1.5$. For comparison, the spectral dependencies of the scattering efficiency η_{scat} on a spherical particle of barium titanate BaTiO₃ and plasmon dimer nanoantenna of gold are given

efficiency for this case Figure 3.5(b). The resulting nanoantenna has a plasmon resonance at the wavelength of 920 nm and two Mie-type resonances at 370 nm and 480 nm. There is also a weakly pronounced resonance at the wavelength equal to 650 nm, arising due to the presence of barium titanate nanoparticle.

Now, when the dielectric and plasmon resonances are in the incident field frequency and SHG frequency, respectively, we can proceed to describe the nonlinear properties of a hybrid Au-BaTiO₃ nanoantenna.

3.2 Second harmonic generation efficiency of a hybrid bi-resonance nanoantenna

After analysing the linear optical response of the hybrid nanoantenna, we turned to studying SHG properties of the proposed antenna. In our approach we considered SHG emission only from dielectric nanoparticle made of barium titanate, while the contribution to the

SHG from gold particles was not taken into account. Indeed, the surface second-order susceptibility of gold $\chi_{surf}^{(2)} \sim 10^{-12}$ cm²/statV is several orders of magnitude lower [63] than the bulk second-order susceptibility $\chi_{bulk}^{(2)} \sim 10^{-8}$ cm/statV of barium titanate.

3.2.1. The influence of the crystalline lattice orientation

To obtain the SHG efficiency spectrum η_{SHG} , we solve the scattering problem in Comsol Multiphysics in the wavelength range from 800 nm to 1200 nm with a step of 10 nm (the direction of the wave vector and electric field are the same as in Section (3.1.2) and it is presented in the Figure 3.6(a)). Then, according to equation (1.17), we calculate the second harmonic generation efficiency η_{SHG} . Having solved the scattering problem on an single particle and on a hybrid nanoantenna, we obtain the spectra shown in the Figure 3.6(b).

It can be seen from the Figure 3.6 that, near 1000 nm, the SHG of the hybrid bi-resonance nanoantenna is two orders of magnitude higher than the SHG of a single BaTiO₃ nanoparticle. The obtained enhancement superior the SHG enhancement by a hybrid dimer nanoantenna, possessing only plasmon resonance at the SHG frequency [21].

Figure 3.6(b) shows the second harmonic generation efficiency η_{SHG} for two orientations of the crystalline lattice: the 1st configuration — the coordinate system attached to the crystalline lattice coincides with the laboratory coordinate system, the 2^d configuration — the coordinate system attached to the crystalline lattice is rotated by $\beta = 45^\circ$ angle around the y-axis (the rotation is described in Section 1.5). Notice, that for the second configuration, the SHG efficiency two orders of magnitude higher relatively to first configuration and the resonance is also slightly shifted to the short-wavelength range.

3.2.2 The influence of the particle position

We fabricate gold dimer antenna consisting of two nanorods with an arm length of $L = 170$ nm, height of $h = 65$ nm, width of $w = 60$ nm

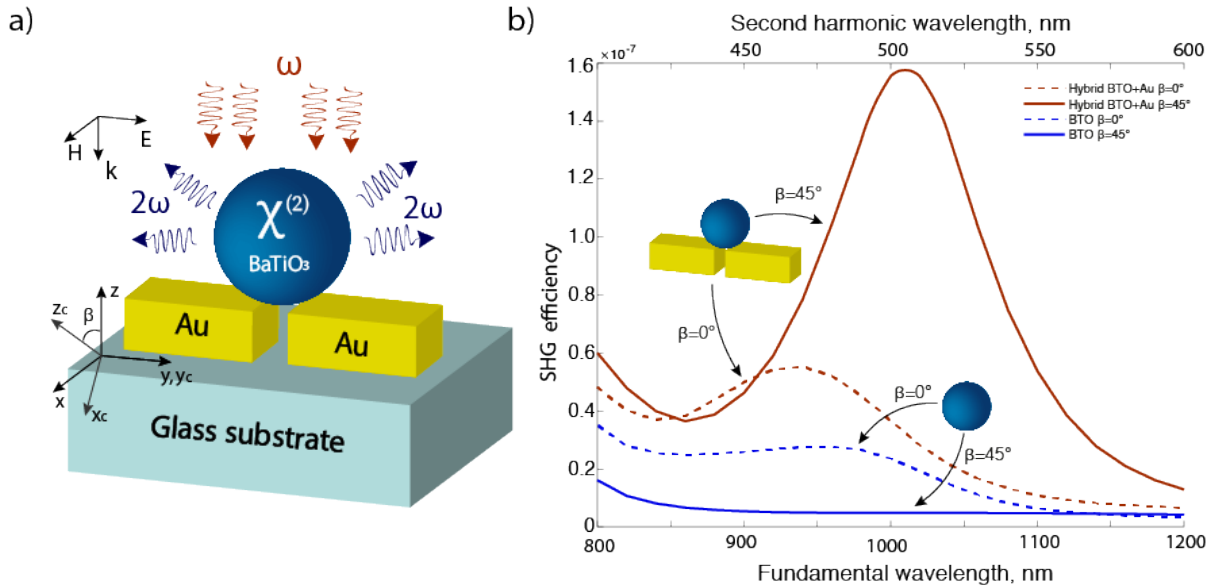


Figure 3.6 — (a) Second harmonic generation on the Au-BaTiO₃ bi-resonant hybrid nanoantenna. (b) Spectral dependence of the second-harmonic generation efficiency η_{SHG} for barium titanate BaTiO₃ and Au-BaTiO₃ hybrid nanoantenna for various angles of rotation of the coordinate system associated with the barium titanate crystal lattice relative to the laboratory coordinate system $\beta = 0^\circ, 45^\circ$ around the y - axis

and a gap of $g = 60$ nm. The lift-off fabrication procedure is described in the Appendix B. Then we use BaTiO₃ nanosphere fabricated by hydrothermal synthesis [64] with a diameter of chosen around 200 nm on the dimer antenna position the BaTiO₃ nanosphere on the dimer nanorod antennas employing a pick-and-place technique described in detail in work [65]. We obtain three hybrid nanodimers, which are name HN1(R8), HN2(M8) and HN3(I8) in the following (see Appendix B for actual sizes of the samples). Figure 3.8 shows the images of the produced nanoantennas in a scanning electron microscope (SEM). It may be noted, that in Figure 3.8, which shows a top view of real structures, the center of the spherical BaTiO₃ nanoparticle is displaced relative to the longitudinal axis of symmetry of the dimer antenna. Let us see how this affects the scattering efficiency and the second harmonic generation efficiency. For this we consider the sample indicated in Figure 3.8 as the HN1(R8), where the center of the spherical nanoparticle is shifted to 96 nm along

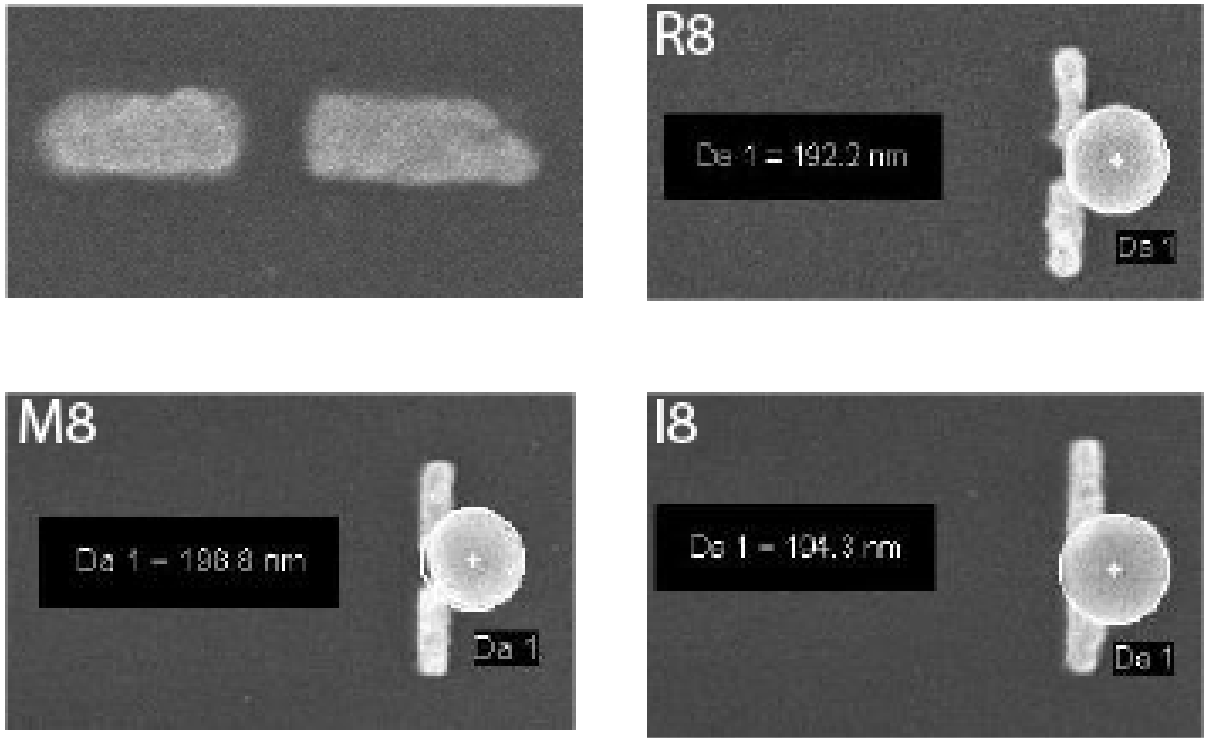


Figure 3.7 — Top view of real structures in a scanning electron microscope

the x-axis and 32 nm down along the z-axis, according to the SEM image. When the BaTiO_3 nanoparticle is shifted to 96 nm along the x-axis and 32 nm down along the z-axis relative to not shifted position we have more pronounced resonance at 370 nm in linear scattering spectrum, otherwise the spectra are very similar in contrast to the second harmonic generation efficiency spectra, where the efficiency strongly depends on both the orientation of the crystalline lattice and the position of the spherical BaTiO_3 nanoparticle. This is due to the fact that the shift changes the symmetry of the system.

3.2.3 Experimental measurement of scattering spectra

Then, we measure the scattering spectrum of the formed hybrid dimers (Figure 3.9(a-c)). Indeed, for each measured hybrid dimer, we detect two resonances, one at around 485 nm, and one at around 1040 nm. We use the FEM model in Comsol Multiphysics to verify the measured spectrum of the hybrid dimers (Figure 3.9(d), here, to comply with conditions analogous to the experiment, namely, the use of unpolarized

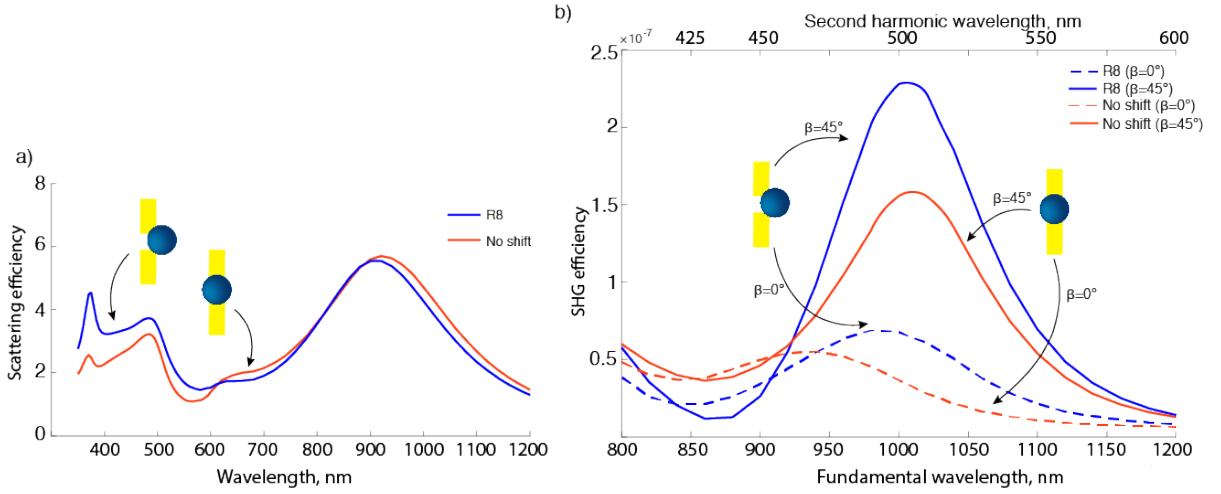


Figure 3.8 — (a) Scattering efficiency η_{scat} depending on fundamental wavelength, blue curve — geometry where the BaTiO_3 nanoparticle is not shifted, red curve — HN1(R8) sample, where the center of the spherical nanoparticle is shifted to 96 nm along the x-axis and 32 nm down along the z-axis relative to not shifted position. (b) Spectral SHG efficiency η_{SHG} for two crystalline lattice orientations: $\beta = 0^\circ$ — dashed curve, $\beta = 45^\circ$ — solid curve; red — not shifted configuration, blue — HN1(R8) sample

pumping, we use the average value of the spectrum for the electric field oscillating along the axis of the dimer antenna and perpendicular to it. The simulations also show two resonances at 485 nm and 920 nm, in excellent agreement with the measurements. The position of the measured LSP resonance is red-shifted in comparison to the calculated value. We explain this variation by the differences between the design of the dimer antenna and the actual size and shape resulting from the fabrication. Specifically, as it can be observed in the Figure 3.8, the fabricated dimer antennas have arms with slightly different arm lengths, their width is not uniform and some surface roughness is present. Furthermore, the ratio between the intensity of the first and second resonance is higher in the measurements compared to the simulations. A possible cause for this difference is the lower sensitivity of the InGaAs camera used for the NIR range compared to the CCD camera used for the visible range.

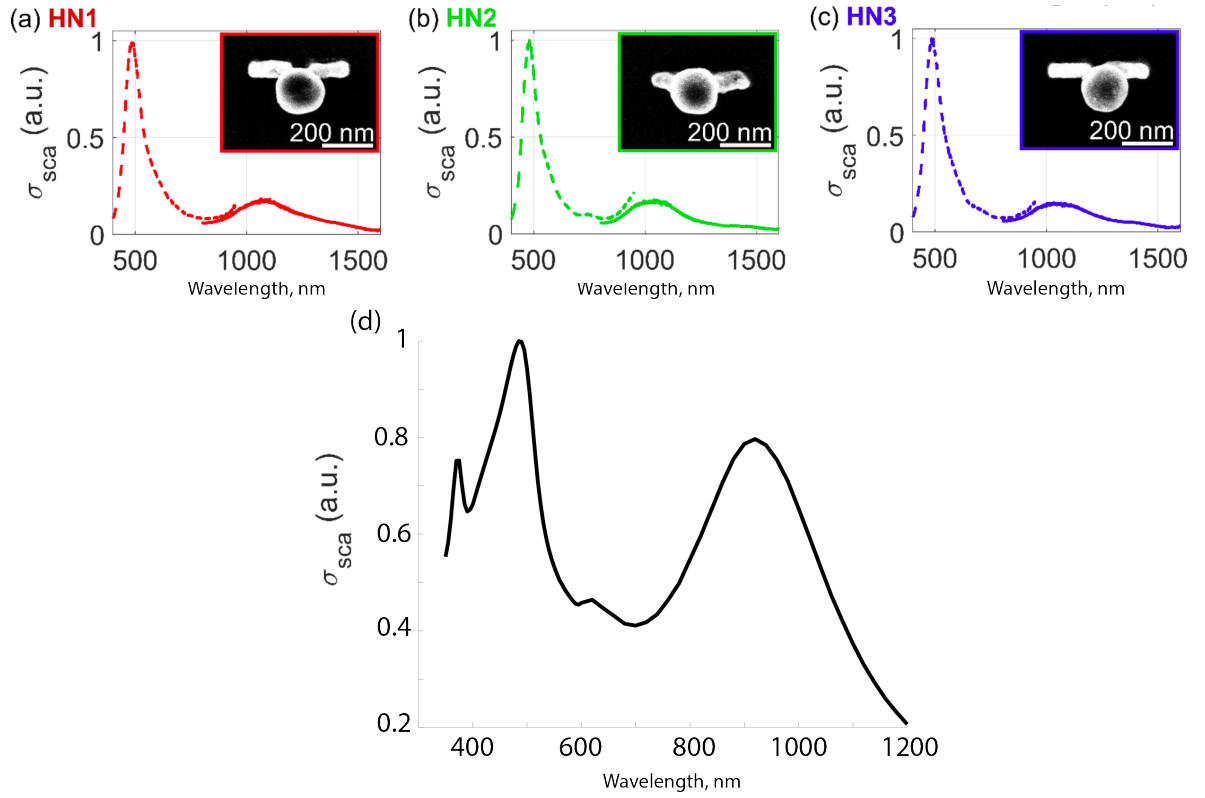


Figure 3.9 — (a-c) Measured linear scattering cross-section of hybrid nanostructures consisting of a BaTiO₃ nanosphere with a diameter of about 200 nm placed on a dimer gold nanorod antenna with an arm length of 170 nm. The hybrid nanostructures are labeled with HN1, HN2 and HN3. The insets show the corresponding SEM micrographs. The spectra shown in dashed lines is detected with a CMOS camera.

The spectra shown with the full line is detected with an InGaAs camera. Data is normalized first by the exposure time and then by the global maximum value over the full detection range. (d) Numerically calculated scattering cross-section of a hybrid nanostructure with similar geometry as HN1-3

3.2.4 Experimental measurement of second harmonic generation efficiency

We compare the measured normalized SHG efficiency of HN(R8) (Figure 3.10(a)) to two single BaTiO₃ nanospheres (Figure 3.10(b)) We observe that, in comparison to single BaTiO₃ nanospheres, the hybrid dimer reach a peak SHG intensity value around 500 nm, which corresponds to an incident laser wavelength of 1000 nm. These

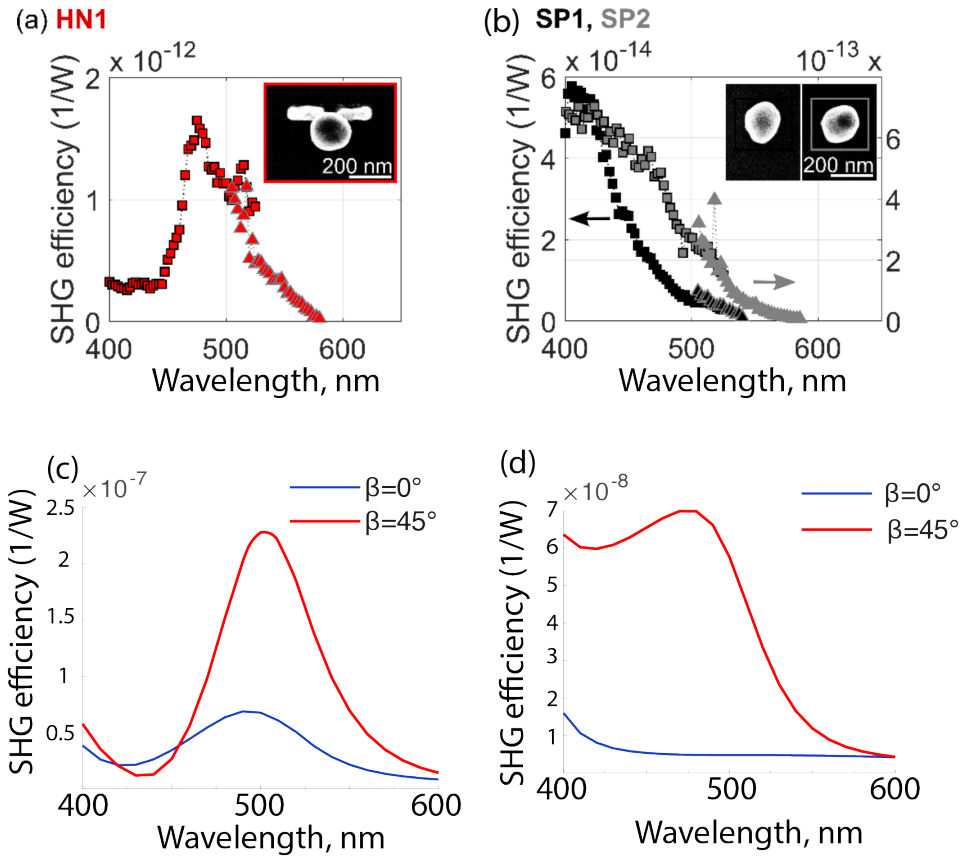


Figure 3.10 — (a) Measured normalized SHG conversion efficiency of the hybrid nanostructure HN1(R8) (b) Measured normalized SHG conversion efficiency of two single BTO nanospheres for comparison. (c-d) Calculated SHG efficiency of a single BaTiO₃ nanospheres (d) with a diameter of 190 nm and a BaTiO₃ nanosphere on a gold dimer antenna (c) for different rotation angles of the BaTiO₃ $\chi^{(2)}$ tensor around the y-axis, $\beta = 0^\circ$ it is orientation, when the axis of the crystal lattice is perpendicular to the substrate

experimental results thus confirm that the presence of the dimer antenna enhances the SHG conversion efficiency of the BaTiO₃ nanosphere. We further investigate the influence of the gold dimer antenna on the SHG conversion efficiency from the BaTiO₃ nanosphere by using a FEM simulation in Comsol Multiphysics of the normalized conversion efficiency from a single BaTiO₃ nanosphere (Figure 3.10(d)) and from a hybrid dimer (Figure 3.10(c)). In the FEM model, we assume that the BaTiO₃ nanosphere is monocrystalline and has the second-order $\chi_{bulk}^{(2)}$. We take into account that the BaTiO₃ nanosphere and the dimer

antenna sit on a glass substrate. Furthermore, we also consider that the BaTiO₃ crystal is rotated by an angle β around the y-axis, $\beta = 0^\circ$ correspond to an orientation perpendicular to the substrate. The orientation of the BaTiO₃ nanosphere and, hence, of the BaTiO₃ crystal, cannot be controlled during the pick-and-place on the dimer antenna. Therefore, we calculate the normalized conversion efficiency for several angles $\beta = 0^\circ$ and $\beta = 45^\circ$ to determine the influence of the BaTiO₃ crystal orientation on the SHG signal. We set the incident electric field to be polarized along the longitudinal axis of the dimer antenna, as in Section 3.1.2.

For the single BaTiO₃ nanospheres (Figure 3.10(d)) and all angles β , the simulation shows that the SHG conversion efficiency is highest at the lower pump wavelength and it generally decreases with the wavelength. However, we also expect a small increase of the SHG conversion efficiency around 500 nm overlapped on the curve decreasing with the wavelength for $\beta = 45^\circ$. This increase corresponds to the SHG enhancement due to the magnetic dipole resonance of the BaTiO₃ nanosphere. In the measured normalized SHG conversion efficiency of single BaTiO₃ nanospheres (Figure 3.10(b)), we do not recover this small peak, but we observe a reduced slope of the SHG conversion efficiency decrease with the wavelength. When we include the dimer antenna in the model, the wavelength dependence of the SHG conversion efficiency changes significantly. For all values of β , the simulation indicates the maximum SHG conversion efficiency to occur at an SHG wavelength corresponding to the half of the LSP resonance wavelength. We obtain this peak in the measured normalized SHG conversion efficiency hybrid nanodimer HN1(R8) (Figure 3.10(a)).

We define the SHG enhancement factor as the ratio of the normalized SHG efficiency of the hybrid dimer and the single BaTiO₃ nanosphere. This factor gives an estimate of the enhancement of the SHG from the BaTiO₃ nanosphere when the dimer antenna is present. For each of the three measured dimers, we obtain enhancement factor values between 2 and 400. For comparison, we also estimate the SHG enhancement factor

from the simulations in Figure 3.10(c-d). We assume that the orientation given by the angle β of the single BaTiO₃ nanosphere and the one on the antenna is not the same. By looking at all possible combinations of angles β , the calculated SHG enhancement factor takes values between 3 and 1500. The value of measured SHG enhancement is well within this interval, with the experimental SHG enhancement factors being generally smaller. This difference is caused by two main factors. First, in the simulations we consider only rotations of the BaTiO₃ $\chi^{(2)}$ tensor around the y-axis. In the experimental context, the BaTiO₃ crystal can be rotated around the two other axes of the laboratory coordinate system, which can lead to an even less favorable orientation of BaTiO₃ with respect to the dimer antenna and the incident electric field vector. The second factor that leads to lower experimental SHG enhancement factors is perhaps not a complete coincidence in parameters of the system and position of the BaTiO₃ nanoparticle between experiment and theory.

Next, we determine numerically and experimentally how the dimer antenna reshapes the SHG emission of the BaTiO₃ nanosphere. To this end, we measure the polar plots of the normalized SHG conversion efficiency. We use the same SHG transmission microscope and we obtain the polar plots by detecting the SHG signal when the polarization of the incident electric field is rotated with a half-wave plate. We show the results for three different SHG wavelengths for the HN1(R8) sample in Figure 3.11(a). We choose the values of 400 nm, 450 nm and 500 nm to observe how the SHG polar plots are reshaped as the incident pump wavelength approaches the longitudinal LSP resonance of the dimer antenna. In numerical calculations, we used two crystalline lattice orientations: $\alpha = 0^\circ$ — oriented perpendicular to the substrate and $\alpha = 45^\circ$ — rotated at α angle around x-axis. Since we cannot control the orientation of the crystalline lattice of barium titanate in the experiment, we numerically investigated several orientations. In Figure 3.11(b-c), you can notice that the polar plots strongly depend on the orientation of the crystalline lattice, and we also have a maximum of SHG, when the incident electric field oscillates along the y-axis — axis of the dimer. which

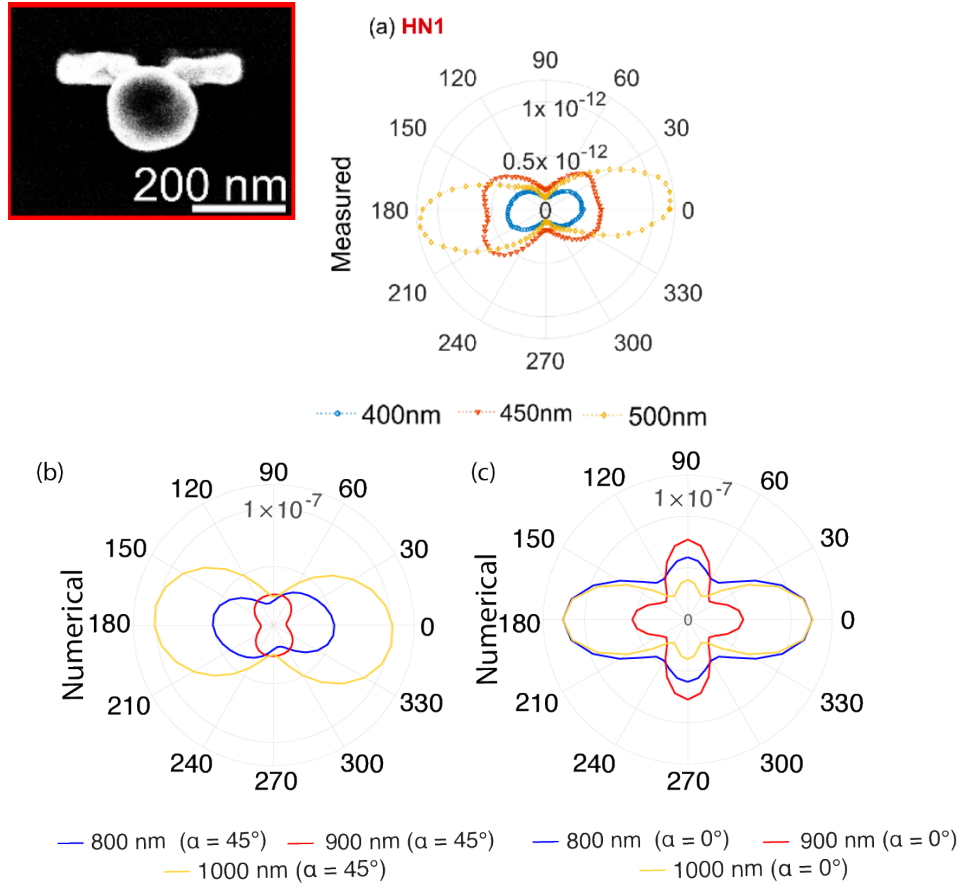


Figure 3.11 — (a) Measured polar plots of the normalized SHG conversion efficiency for the hybrid nanostructure HN1(R8) for three SHG wavelengths: 400 nm — blue circle, 450 nm — orange triangle, 500 nm — yellow diamonds. (b-c) Calculated polar plots of the SHG efficiency for the same SHG wavelengths: 400 nm — blue lines, 450 nm — orange lines, 500 nm — yellow lines. The crystalline lattice is rotated at $\alpha = 45^\circ$ (b) and $\alpha = 0^\circ$ (c) angle around the x-axis

is logical, since in such a configuration there is plasmon resonance at a frequency of 1000 nm. This is explained by the fact that in such a configuration, at a doubled frequency of the second harmonic generation, there is a plasmon resonance. At angle $\alpha = 45^\circ$, we obtained numerical polar plots similar to experimental ones, however, in the experiment, the SHG efficiency increases with the increasing wavelengths from 400 nm to 500 nm, and in numerical calculations we see a decrease in efficiency at a wavelength of 450 nm, This is due to the fact that, in numerical

calculations (Figure 3.10(c)), the spectrum is slightly shifted to the long-wavelength range, relative to experimental data (Figure 3.10(a)).

4 CONNECTION BETWEEN SPONTANEOUS DOWN-CONVERSION AND SECOND HARMONIC GENERATION

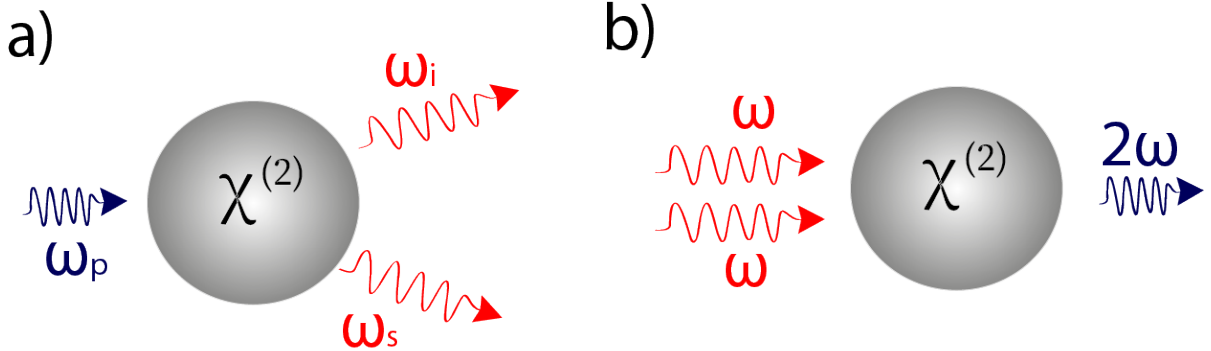


Figure 4.1 — (a) Scheme of spontaneous parametric down-conversion: a photon with a frequency ω_p is incident on the particle with a second-order bulk non-linearity $\chi_{bulk}^{(2)} \neq 0$ and decays into two signal and idler photons, with frequencies ω_i , and ω_s , respectively, the energy conservation law is fulfilled $\omega_i + \omega_s = \omega_p$. (b) Scheme of second harmonic generation: two photon with same frequency ω are interact with the particle with a second-order bulk non-linearity $\chi_{bulk}^{(2)} \neq 0$ and generate new photon with higher frequency 2ω

As it was shown earlier in Section 2.2, the process of SPDC and in particular a two-photon amplitude determined by the overlapping integrals (eq. 2.4) between the mode of the pump field \mathbf{W}_{J_p} and decay modes \mathbf{W}_{J_i} and \mathbf{W}_{J_s} . For clarity, we represent these coefficients again

$$D_{J_p \rightarrow J_i, J_s} = \sum_{\alpha, \beta, \gamma} \chi_{\alpha\beta\gamma} \int_V W_{J_p, \gamma}(\omega_p, \mathbf{r}_0) W_{J_i, \alpha}(\omega_i, \mathbf{r}_0) W_{J_s, \beta}(\omega_s, \mathbf{r}_0) d^3 r_0. \quad (4.1)$$

In the works [55, 66], it was shown that the intensity of the second harmonic generation $I_{2\omega}$ as a coherent process is determined by the cross density of states [67]:

$$I_{2\omega} = \frac{(2\omega)^3 \mu \mu_0}{2} \int \int dV' dV'' \mathbf{P}^*(\mathbf{r}', 2\omega, \omega) \mathfrak{S}[\hat{G}(\mathbf{r}', \mathbf{r}'', 2\omega)] \mathbf{P}(\mathbf{r}'', 2\omega, \omega),$$

where $P_i(\mathbf{r}, 2\omega, \omega) = \chi_{ijk}^{(2)} E_{p,j}(\mathbf{r}, \omega) E_{p,k}(\mathbf{r}, \omega)$. The intensity of the SHG is proportional to the sum of the squares of the D-coefficients, $I_{2\omega} \sim \sum |D_{\mathbf{J}, \mathbf{J}' \rightarrow \mathbf{J}''}|^2$, which are identical overlapping integrals as for the SPDC process, but in this case, between two pump modes $\mathbf{W}_{\mathbf{J}}, \mathbf{W}_{\mathbf{J}'}$ and one mode at double frequency $\mathbf{W}_{\mathbf{J}''}$:

$$D_{\mathbf{J}, \mathbf{J}' \rightarrow \mathbf{J}''} = \sum_{\alpha, \beta, \gamma} \chi_{\alpha\beta\gamma} \int_V W_{\mathbf{J}'', \gamma}(2\omega, \mathbf{r}_0) W_{\mathbf{J}, \alpha}(\omega, \mathbf{r}_0) W_{\mathbf{J}', \beta}(\omega, \mathbf{r}_0) d^3 r_0. \quad (4.2)$$

Thus, by analyzing the expressions 4.1 and 4.2, we obtain one more tight connection between inverse processes (Figure 4.1), which is which is not quite obvious at first glance, but shows, that these two processes have the similar selection rules, depending on the nanoparticle's and lattice symmetries. This connection is very important, since nonlinear properties are highly dependent on the selection rules, which can be now applicable to higher variety of cases.

CONCLUSION

In this work, we investigated second-order nonlinear processes in all-dielectric and hybrid metal-dielectric nanostructures. We have obtained a connection between spontaneous parametric down-conversion (SPDC) and second harmonic generation (SHG) through similar overlapping integrals and get the same selection rules for such integrals. In the first part of the work, we theoretically study the degenerate SPDC of light by a subwavelength dielectric spherical particle based on materials without inversion center, having a non-zero second-order susceptibility tensor $\chi_{bulk}^{(2)}$. The following results were obtained:

- analytic expression for the two-photon amplitude of bi-photons generated by a spherical nanoparticle during SPDC in the framework of the Mie theory;
- directional Kerker-type nonlinear generation of photon pairs is observed and general conditions are obtained for observing such generation in the collinear decay;
- the polarization correlations between the signal and idler photons are investigated in case of wurtzite type gallium arsenide GaAs nanosphere.

In the second part of the work, we propose a hybrid nanostructure consisting of a gold dimer nanorod antenna and a BaTiO₃ nanosphere. We design this hybrid nanostructure such that the longitudinal localized surface plasmon resonance (LSPR) of the dimer antenna occurs at the double wavelength of the Mie resonance of the BaTiO₃ nanoparticle. The role of the LSPR is to couple the pump efficiently to the nanostructure through the formation of a hot-spot between the antenna arms, where the BaTiO₃ nanoparticle is located. In turn, the Mie resonance of the BaTiO₃ improves the SHG radiation to the far-field. The following results were obtained:

- the system parameters are numerically selected for the presence of two resonances: localized surface plasmon resonance at the fundamental

wavelength 1000 nm and Mie resonance at the wavelength of 500 nm, corresponding to second harmonic generation. Then, based on these parameters, several samples were made for the experiment, using e-beam lithography and nanopositioning of BaTiO₃ nanoparticle;

— numerically and experimentally obtained enhancement of second harmonic generation efficiency by hybrid bi-resonance Au-BaTiO₃ structure up to $10^2 - 10^3$ times of magnitude higher relative to a single spherical barium titanate nanoparticle;

— it has been demonstrated that the SHG efficiency strongly depends on the orientation of the crystalline lattice relative to the incident field, as well as on the position of the barium titanate nanoparticle relative to the gold dimer nanoantenna.

REFERENCES

1. Plasmon lasers at deep subwavelength scale / Rupert F. Oulton, Volker J. Sorger, Thomas Zentgraf et al. // *Nature*. — 2009. — Vol. 461, no. 7264. — Pp. 629–632.
2. *Butet, Jeremy*. Optical Second Harmonic Generation in Plasmonic Nanostructures: From Fundamental Principles to Advanced Applications / Jeremy Butet, Pierre-Franchois Brevet, Olivier J. F. Martin // *ACS Nano*. — 2015. — Vol. 9, no. 11. — Pp. 10545–10562.
3. Optically resonant dielectric nanostructures / Arseniy I. Kuznetsov, Andrey E. Miroshnichenko, Mark L. Brongersma et al. // *Science*. — 2016. — Vol. 354, no. 6314. — P. 2472.
4. *Jahani, Saman*. All-dielectric metamaterials / Saman Jahani, Zubin Jacob // *Nature nanotechnology*. — 2016. — Vol. 11, no. 1. — Pp. 23–36.
5. Strong magnetic response of submicron Silicon particles in the infrared / A. García-Etxarri, R. Gómez-Medina, L. S. Froufe-Pérez et al. // *Optics Express*. — 2011. — Vol. 19, no. 6. — P. 4815.
6. *Kuznetsov, Arseniy I*. Magnetic light. — 2012.
7. *Sain, Basudeb*. Nonlinear optics in all-dielectric nanoantennas and metasurfaces: a review / Basudeb Sain, Cedrik Meier, Thomas Zentgraf // *Advanced Photonics*. — 2019. — Vol. 1, no. 02. — P. 1.
8. Enhanced third-harmonic generation in silicon nanoparticles driven by magnetic response / Maxim R. Shcherbakov, Dragomir N. Neshev, Ben Hopkins et al. // *Nano Letters*. — 2014. — Vol. 14, no. 11. — Pp. 6488–6492.
9. Multifold enhancement of third-harmonic generation in dielectric nanoparticles driven by magnetic Fano resonances / Alexander S. Shorokhov, Elizaveta V. Melik-Gaykazyan, Daria a. Smirnova et al. // *Nano Lett*. — 2016. — Vol. 16. — Pp. 4857–4861.
10. Third-harmonic generation from Mie-type resonances of isolated all-dielectric nanoparticles Subject Areas : Author for corre-

spondence : / Elizaveta V Melik-gaykazyan, Maxim R Shcherbakov, Alexander S Shorokhov et al. // *Philosophical Transactions of the Royal Society A: Mathematical, Physical and Engineering Sciences*. — 2017. — Vol. 375. — P. 20160281.

11. Ultrafast All-Optical Switching with Magnetic Resonances in Nonlinear Dielectric Nanostructures / Maxim R. Shcherbakov, Polina P. Vabishchevich, Alexander S. Shorokhov et al. // *Nano Letters*. — 2015. — Vol. 15, no. 10. — Pp. 6985–6990.

12. Tuning of Magnetic Optical Response in a Dielectric Nanoparticle by Ultrafast Photoexcitation of Dense Electron–Hole Plasma / Sergey Makarov, Sergey Kudryashov, Ivan Mukhin et al. // *Nano Letters*. — 2015. — Vol. 15, no. 9. — Pp. 6187–6192.

13. *Maier, Stefan A.* Plasmonics: Fundamentals and applications / Stefan A. Maier. — 2007. — Pp. 1–223.

14. *Boardman, A. D.* Nonlinear plasmonics / A. D. Boardman, A. V. Zayats // *Handbook of Surface Science*. — 2014. — Vol. 4. — Pp. 329–347.

15. Enhanced second-harmonic generation from double resonant plasmonic antennae. / Krishnan Thyagarajan, Simon Rivier, Andrea Lovera, Olivier J F Martin // *Optics express*. — 2012. — Vol. 20, no. 12. — Pp. 12860–5.

16. Enhancement Mechanisms of the Second Harmonic Generation from Double Resonant Aluminum Nanostructures / Kuang Yu Yang, Jérémy Butet, Chen Yan et al. // *ACS Photonics*. — 2017. — Vol. 4, no. 6. — Pp. 1522–1530.

17. *Butet, Jérémy.* Optical Second Harmonic Generation in Plasmonic Nanostructures: From Fundamental Principles to Advanced Applications / Jérémy Butet, Pierre-François Brevet, Olivier J. F. Martin // *ACS Nano*. — 2015. — Vol. 9, no. 11. — Pp. 10545–10562.

18. Towards all-dielectric metamaterials and nanophotonics / V. Kuzmiak, A. Krasnok, S. Makarov et al. // *Proceedings of SPIE - The International Society for Optical Engineering*. — Vol. 9502. —

2015.

19. *Aspnes, D. E.* Dielectric functions and optical parameters of Si, Ge, GaP, GaAs, GaSb, InP, InAs, and InSb from 1.5 to 6.0 eV / D. E. Aspnes, A. A. Studna // *Physical Review B*. — 1983. — Vol. 27, no. 2. — Pp. 985–1009.

20. Efficient Second-Harmonic Generation in Nanocrystalline Silicon Nanoparticles / Sergey V. Makarov, Mihail I. Petrov, Urs Zywiets et al. // *Nano Letters*. — 2017. — Vol. 17, no. 5. — Pp. 3047–3053.

21. Enhanced Second-Harmonic Generation from Sequential Capillarity-Assisted Particle Assembly of Hybrid Nanodimers / Flavia Timpu, Nicholas R. Hendricks, Mihail Petrov et al. // *Nano Letters*. — 2017. — Vol. 17, no. 9. — Pp. 5381–5388.

22. Enhanced second-harmonic generation from magnetic resonance in AlGaAs nanoantennas. / L Carletti, A Locatelli, O Stepanenko et al. // *Optics express*. — 2015. — Vol. 23, no. 20. — Pp. 26544–50.

23. Anapoles in Free-Standing III-V Nanodisks Enhancing Second-Harmonic Generation / Maria Timofeeva, Lukas Lang, Flavia Timpu et al. // *Nano Letters*. — 2018. — Vol. 18. — Pp. 3695–3702.

24. Bridging the gap between dielectric nanophotonics and the visible regime with effectively lossless GaP antennas / Javier Cambiasso, Gustavo Grinblat, Yi Li et al. // *Nano Letters*. — 2017. — Vol. 17. — Pp. 1219–1225.

25. Nonlinear Generation of Vector Beams from AlGaAs Nanoantennas / Rocio Camacho-Morales, Mohsen Rahmani, Sergey Kruk et al. // *Nano Letters*. — 2016. — Vol. 16, no. 11. — Pp. 7191–7197.

26. Polarization-Dependent Second Harmonic Diffraction from Resonant GaAs Metasurfaces / Franz Löchner, Anna N. Fedotova, Sheng Liu et al. // *ACS Photonics*. — 2018. — P. 01533.

27. Giant nonlinear response at the nanoscale driven by bound states in the continuum / Luca Carletti, Kirill Koshelev, Costantino De Angelis, Yuri Kivshar. — 2018. — Vol. 2, no. 1. — Pp. 1–7.

28. Subwavelength dielectric resonators for nonlinear nanophotonics / Kirill Koshelev, Sergey Kruk, Elizaveta Melik-Gaykazyan et al. // *Science*. — 2020. — Vol. 367, no. 6475. — Pp. 288–292.
29. *Smirnova, Daria*. Multipolar nonlinear nanophotonics / Daria Smirnova, Yuri S. Kivshar // *Optica*. — 2016. — Vol. 3, no. 11. — P. 1241.
30. Forward and Backward Switching of Nonlinear Unidirectional Emission from GaAs Nanoantennas / Lei Xu, Grégoire Saerens, Maria Timofeeva et al. // *ACS Nano*. — 2020. — Vol. 14, no. 2. — Pp. 1379–1389.
31. On-demand generation of indistinguishable polarization-entangled photon pairs / M. Muller, S. Bounouar, K. D. Jons et al. // *Nature Photonics*. — 2014. — Mar. — Vol. 8, no. 3. — Pp. 224–228.
32. Observation of strongly entangled photon pairs from a nanowire quantum dot / M. A. M. Versteegh, M. E. Reimer, K. D. Jons et al. // *Nature Communications*. — 2014. — Oct. — Vol. 5. — Pp. 5298–6.
33. *Solntsev, A. S.* Path-entangled photon sources on nonlinear chips / A. S. Solntsev, A. A. Sukhorukov // *RPH*. — 2017. — Vol. 2. — Pp. 19–31.
34. *O'Brien, J. L.* Photonic quantum technologies / J. L. O'Brien, A. Furusawa, J. Vučković // *Nature Photonics*. — 2009. — Dec. — Vol. 3, no. 12. — Pp. 687–695.
35. LiNbO₃ waveguides for integrated SPDC spectroscopy / A. S. Solntsev, P. Kumar, T. Pertsch et al. // *APLP*. — 2018. — Feb. — Vol. 3, no. 2. — Pp. 021301–8.
36. *Oka, Hisaki*. Generation of broadband ultraviolet frequency-entangled photons using cavity quantum plasmonics / Hisaki Oka // *Scientific Reports*. — 2017. — Vol. 7, no. 1. — Pp. 1–10.
37. Entangled light from bimodal optical nanoantennas / J. Straubel, R. Sarniak, C. Rockstuhl, K. Słowik // *Physical Review B*. — 2017. — Vol. 95, no. 8. — Pp. 1–9.

38. *Biehs, S. A.* Qubit entanglement across ε -near-zero media / S. A. Biehs, G. S. Agarwal // *Physical Review A*. — 2017. — Vol. 96, no. 2. — Pp. 1–8.
39. Tunable multi-qubit quantum phase gates with high fidelity based on graphene wrapped particle / Jun Ren, Weixuan Zhang, Bing Yang, Xiangdong Zhang // *AIP Advances*. — 2016. — Vol. 6, no. 11.
40. Spontaneous photon-pair generation from a dielectric nanoantenna / Giuseppe Marino, Alexander S. Solntsev, Lei Xu et al. // *Optica*. — 2019. — Vol. 6, no. 11. — P. 1416.
41. Hybrid nanoantennas for directional emission enhancement / Evgenia Rusak, Isabelle Staude, Manuel Decker et al. // *Applied Physics Letters*. — 2014. — Vol. 105, no. 22.
42. Fabrication of Hybrid Nanostructures via Nanoscale Laser-Induced Reshaping for Advanced Light Manipulation / Dmitry A. Zuev, Sergey V. Makarov, Ivan S. Mukhin et al. // *Advanced Materials*. — 2016. — Vol. 28, no. 16. — Pp. 3087–3093.
43. Second harmonic generation spectroscopy on hybrid plasmonic / dielectric nanoantennas / Heiko Linnenbank, Yevgen Grynko, Jens Förstner, Stefan Linden // *Light: Science and Applications*. — 2015. — Vol. submitted, no. April 2015. — Pp. 1–7.
44. Metal-Dielectric Hybrid Dimer Nanoantenna: Coupling between Surface Plasmons and Dielectric Resonances for Fluorescence Enhancement / Song Sun, Mo Li, Qingguo Du et al. // *Journal of Physical Chemistry C*. — 2017. — Vol. 121, no. 23. — Pp. 12871–12884.
45. Nonlinear optical properties of core-shell nanocavities for enhanced second-harmonic generation / Ye Pu, Rachel Grange, Chia Lung Hsieh, Demetri Psaltis // *Physical Review Letters*. — 2010. — may. — Vol. 104, no. 20. — Pp. 207401–207405.
46. Inverse Designed Metalenses with Extended Depth of Focus / Elyas Bayati, Raphaël Pestourie, Shane Colburn et al. // *ACS Photonics*. — 2020. — Vol. 7, no. 4. — Pp. 873–878.

47. Reshaping the Second-Order Polar Response of Hybrid Metal-Dielectric Nanodimers / Claude Renaut, Lukas Lang, Kristina Frizyuk et al. // *Nano Letters*. — 2019. — Vol. 19, no. 2. — Pp. 877–884.
48. Second-harmonic generation with metal/dielectric/metal hybridized nanoantennas: Enhanced efficiency, reduced mode volume and ideal magnetic/electric dipole scattering / Hong Gang Hu, Min Yang, Peng Yue et al. // *Journal of Physics D: Applied Physics*. — 2020. — Vol. 53, no. 21.
49. *Poddubny, Alexander N.* Generation of Photon-Plasmon Quantum States in Nonlinear Hyperbolic Metamaterials / Alexander N. Poddubny, Ivan V. Iorsh, Andrey A. Sukhorukov // *Physical Review Letters*. — 2016. — Vol. 117, no. 12. — Pp. 1–6.
50. *Bohren, C.* Absorption and Scattering of Light by Small Particles / C. Bohren, D. R. Huffman; Ed. by C. Bohren, D. R. Huffman. — Wiley Science Paperback Series, 1998.
51. *Bradford Mason, V.* The Electromagnetic Radiation from Simple Sources in the Presence of a Homogenous Dielectric Sphere. — 1972.
52. *Cabuk, Suleyman.* The nonlinear optical susceptibility and electro-optic tensor of ferroelectrics: first-principle study / Suleyman Cabuk // *Open Physics*. — 2012. — Vol. 10, no. 1.
53. Polar Second-Harmonic Imaging to Resolve Pure and Mixed Crystal Phases along GaAs Nanowires / Maria Timofeeva, Alexei Bouravleuv, George Cirlin et al. // *Nano Letters*. — 2016. — Vol. 16, no. 10. — Pp. 6290–6297.
54. Directional visible light scattering by silicon nanoparticles / Yuan Hsing Fu, Arseniy I. Kuznetsov, Andrey E. Miroshnichenko et al. // *Nature Communications*. — 2013. — Vol. 4. — Pp. 1–6.
55. Second-harmonic generation in Mie-resonant dielectric nanoparticles made of noncentrosymmetric materials / Kristina Frizyuk, Irina Volkovskaya, Daria Smirnova et al. // *Physical Review B*. — 2019. — Vol. 99, no. 7. — Pp. 1–18.

56. Forward and Backward Switching of Nonlinear Unidirectional Emission from GaAs Nanoantennas / Lei Xu, Grégoire Saerens, Maria Timofeeva et al. // *ACS Nano*. — 2020. — Vol. 14, no. 2. — Pp. 1379–1389.

57. Interfacing a two-photon NOON state with an atomic quantum memory / Wei Zhang, Ming-Xin Dong, Dong-Sheng Ding et al. // *Phys. Rev. A*. — 2018. — Dec. — Vol. 98. — P. 063820.

58. Wave-Mixing Origin and Optimization in Single and Compact Aluminum Nanoantennas / Maëliiss Ethis de Corny, Nicolas Chauvet, Guillaume Laurent et al. // *ACS Photonics*. — 2016. — Vol. 3, no. 10. — Pp. 1840–1846.

59. Evidence of Cascaded Third-Harmonic Generation in Noncentrosymmetric Gold Nanoantennas / Michele Celebrano, Andrea Locatelli, Lavinia Ghirardini et al. // *Nano Letters*. — 2019. — Vol. 19, no. 10. — Pp. 7013–7020.

60. *Babar, Shaista*. Optical constants of Cu, Ag, and Au revisited / Shaista Babar, J. H. Weaver // *Appl. Opt.* — 2015. — Jan. — Vol. 54, no. 3. — Pp. 477–481.

61. Optical scattering resonances of single and coupled dimer plasmonic nanoantennas / O. L. Muskens, V. Giannini, J. A. Sánchez-Gil, J. Gómez Rivas // *Opt. Express*. — 2007. — Dec. — Vol. 15, no. 26. — Pp. 17736–17746.

62. Unmodified hot spot in hybridized nanorod dimer for extended surface-enhanced Raman scattering // *Journal of Physics and Chemistry of Solids*. — 2020. — Vol. 136. — P. 109125.

63. *Krause, Debra*. Optical surface second harmonic measurements of Isotropic thin-film metals: Gold, silver, copper, aluminum, and tantalum / Debra Krause, Chartes W. Teplin, Charles T. Rogers // *Journal of Applied Physics*. — 2004. — Vol. 96, no. 7. — Pp. 3626–3634.

64. Synthesis of BaTiO₃ Particles with Tailored Size by Precipitation from Aqueous Solutions / Andrea Testinon, Maria Teresa Buscaglia, Massimo Viviani et al. // *Journal of the American Ceramic Society*. — Vol. 87, no. 1. — Pp. 79–83.

65. Reshaping the Second-Order Polar Response of Hybrid Metal–Dielectric Nanodimers / Claude Renault, Lukas Lang, Kristina Frizyuk et al. // *Nano Letters*. — 2019. — Vol. 19, no. 2. — Pp. 877–884.

66. Second harmonic generation and spontaneous parametric down-conversion in Mie nanoresonators / M I Petrov, A A Nikolaeva, K S Frizyuk, N A Olekhno // *Journal of Physics: Conference Series*. — 2018. — dec. — Vol. 1124. — P. 051021.

67. Cazé, A. Spatial Coherence in Complex Photonic and Plasmonic Systems / A. Cazé, R. Pierrat, R. Carminati // *Phys. Rev. Lett.* — 2013. — Feb. — Vol. 110. — P. 063903.

APPENDIX A

Linear Kerker effect

Let's obtain the expression 2.1

$$\begin{aligned}
 |\mathbf{S}| &\simeq |\mathbf{E}_s|^2 = |E_1|^2 (ia_1 \mathbf{N}_x^{(1)} - b_1 \mathbf{M}_y^{(1)}) (-ia_1^* \mathbf{N}_x^{(1)*} - b_1^* \mathbf{M}_y^{(1)*}) =^{(1)} \quad (\text{A.1}) \\
 &= |E_1|^2 \left[|a_1|^2 |\mathbf{N}_x^{(1)}|^2 + |b_1|^2 |\mathbf{M}_y^{(1)}|^2 + 2\Re(ia_1^* b_1 \mathbf{N}_x^{(1)*} \mathbf{M}_y^{(1)}) \right] \\
 &= |E_1|^2 \left[|a_1|^2 |\mathbf{N}_x^{(1)}|^2 + |b_1|^2 |\mathbf{M}_y^{(1)}|^2 - 2\Im(a_1^* b_1 \mathbf{N}_x^{(1)*} \mathbf{M}_y^{(1)}) \right]
 \end{aligned}$$

Next, we use multiple identities such as

$$\begin{aligned}
 \Im(ab) &= \Re(a)\Im(b) + \Re(b)\Im(a) \\
 \Re(a^*b) &= |a^*b| \cos(\varphi_b - \varphi_a) \\
 \Im(a^*b) &= |a^*b| \sin(\varphi_b - \varphi_a)
 \end{aligned}$$

After substitution we get

$$\begin{aligned}
 |\mathbf{S}| &\simeq |E_1|^2 \left[|a_1|^2 |\mathbf{N}_x^{(1)}|^2 + |b_1|^2 |\mathbf{M}_y^{(1)}|^2 - \right. \\
 &\quad \left. -2|a_1^* b_1 \mathbf{N}_x^{(1)*} \mathbf{M}_y^{(1)}| \cos(\varphi_{b_1} - \varphi_{a_1}) \sin(\varphi_{M_y} - \varphi_{N_x}) - \right. \\
 &\quad \left. -2|a_1^* b_1 \mathbf{N}_x^{(1)*} \mathbf{M}_y^{(1)}| \cos(\varphi_{M_y} - \varphi_{N_x}) \sin(\varphi_{b_1} - \varphi_{a_1}) \right]
 \end{aligned}$$

Using the asymptotics of spherical Hankel functions in the far field and expressions for vector spherical harmonics (eq.1.4-1.7), we can consider the phase difference $\varphi_{M_y} - \varphi_{N_x}$ at the points $\theta = 0, \pi: (\varphi_{M_y} - \varphi_{N_x})|_{\theta=0} = -\pi/2$ and $(\varphi_{M_y} - \varphi_{N_x})|_{\theta=\pi} = \pi/2$.

$$\begin{aligned}
 h_n^{(1)}(\rho) &\sim \frac{(-i)^n e^{i\rho}}{\rho} \\
 \frac{1}{\rho} \frac{d}{d\rho} [\rho h_n^{(1)}(\rho)] &\sim \frac{(-i)^n e^{i\rho}}{\rho}
 \end{aligned}$$

Collinear directional generation

Consider a little more detailed expression 2.6 and its output. First, we'll show how we summed up over \mathbf{d}_i and \mathbf{d}_s in expression 2.5:

$$\begin{aligned}
w_{is}^{unpol}(\mathbf{r}_i, \omega_i; \mathbf{r}_s, \omega_s) &\sim \sum_{\mathbf{d}_i, \mathbf{d}_s} |T_{is}(\mathbf{r}_i, \omega_i, \mathbf{d}_i; \mathbf{r}_s, \omega_s, \mathbf{d}_s)|^2 \\
&\sim \sum_{\mathbf{d}_i, \mathbf{d}_s} \sum_{\substack{\mathbf{J}_p, \mathbf{J}_i, \mathbf{J}_s \\ \mathbf{J}'_p, \mathbf{J}'_i, \mathbf{J}'_s}} \underbrace{\tilde{T}_{\mathbf{J}_p \rightarrow \mathbf{J}_i, \mathbf{J}_s} \cdot D_{\mathbf{J}_p \rightarrow \mathbf{J}_i, \mathbf{J}_s} \cdot \tilde{T}_{\mathbf{J}'_p \rightarrow \mathbf{J}'_i, \mathbf{J}'_s}^* \cdot D_{\mathbf{J}'_p \rightarrow \mathbf{J}'_i, \mathbf{J}'_s}^*}_{C_{\mathbf{J}'_p \rightarrow \mathbf{J}'_i, \mathbf{J}'_s}^{\mathbf{J}_p \rightarrow \mathbf{J}_i, \mathbf{J}_s}} \times \left(\mathbf{d}_i^* \cdot \mathbf{W}_{\mathbf{J}_i}^{(1)}(k_{i1}, \mathbf{r}_i) \right) \times \\
&\quad \times \left(\mathbf{W}_{\mathbf{J}_s}^{(1)}(k_{s1}, \mathbf{r}_s) \cdot \mathbf{d}_s^* \right) \times \left(\mathbf{d}_i \cdot \mathbf{W}_{\mathbf{J}'_i}^{*(1)}(k_{i1}, \mathbf{r}_i) \right) \left(\mathbf{W}_{\mathbf{J}'_s}^{*(1)}(k_{s1}, \mathbf{r}_s) \cdot \mathbf{d}_s \right).
\end{aligned}$$

Since we summarize over all possible polarizations $\mathbf{d}_{i(s)} = d_{i(s)} \mathbf{e}_\alpha$, where $\alpha = x, y, z$, we can assume that the scalar product $\mathbf{d}_{i(s)}^* \cdot \mathbf{W}_{\mathbf{J}_{i(s)}}^{(1)}$ is the projection of the vector $\mathbf{W}_{\mathbf{J}_{i(s)}}^{(1)}$ on the α -axis $W_{\mathbf{J}_{i(s)}, \alpha}^{(1)}$. In this way,

$$\sum_{\mathbf{d}_i} (\mathbf{d}_i^* \cdot \mathbf{W}_{\mathbf{J}_i}^{(1)}) (\mathbf{d}_i \cdot \mathbf{W}_{\mathbf{J}'_i}^{(1)*}) = \sum_{\alpha} W_{\mathbf{J}_i, \alpha}^{(1)} W_{\mathbf{J}'_i, \alpha}^{(1)*} = \mathbf{W}_{\mathbf{J}_i}^{(1)} \cdot \mathbf{W}_{\mathbf{J}'_i}^{(1)*}.$$

Hence,

$$\begin{aligned}
w_{is}^{unpol}(\mathbf{r}_i, \omega_i; \mathbf{r}_s, \omega_s) &\sim \sum_{\substack{\mathbf{J}_p, \mathbf{J}_i, \mathbf{J}_s \\ \mathbf{J}'_p, \mathbf{J}'_i, \mathbf{J}'_s}} C_{\mathbf{J}'_p \rightarrow \mathbf{J}'_i, \mathbf{J}'_s}^{\mathbf{J}_p \rightarrow \mathbf{J}_i, \mathbf{J}_s} \left(\mathbf{W}_{\mathbf{J}_i}^{(1)}(k_{i1}, \mathbf{r}_i) \cdot \mathbf{W}_{\mathbf{J}'_i}^{*(1)}(k_{i1}, \mathbf{r}_i) \right) \times \\
&\quad \times \left(\mathbf{W}_{\mathbf{J}_s}^{(1)}(k_{s1}, \mathbf{r}_s) \cdot \mathbf{W}_{\mathbf{J}'_s}^{*(1)}(k_{s1}, \mathbf{r}_s) \right) \quad (\text{A.2})
\end{aligned}$$

Analyzing the terms in the expression A.2, we can understand that part of the terms will contribute to $w^{unpol}|_{\theta=0, \pi}$, but will not give directivity, we denote them as w_0^{unpol} , also part of the terms will contribute to the directivity. Let's look at all possible scalar products $|\mathbf{W}_{\mathbf{J}} \cdot \mathbf{W}_{\mathbf{J}'}|$ in Figure A.1 and note that the contributions into $w^{unpol}|_{\theta=0, \pi}$ will only give the products $|\mathbf{M}_y|^2$, $|\mathbf{N}_x|^2$ and $|\mathbf{M}_y \cdot \mathbf{N}_x|$, therefore, we will consider only them in A.2 (similarly for $|\mathbf{N}_y|^2$, $|\mathbf{M}_x|^2$ and $|\mathbf{N}_y \cdot \mathbf{M}_x|$, but let's throw them away for brevity). Obviously, the expression w_0^{unpol} will include terms proportional to $\sim (D_{\mathbf{N}_x \rightarrow \mathbf{N}_x, \mathbf{N}_x})^2$, $\sim (D_{\mathbf{N}_x \rightarrow \mathbf{M}_y, \mathbf{M}_y})^2$, $\sim (D_{\mathbf{M}_y \rightarrow \mathbf{M}_y, \mathbf{N}_x})^2$ and $\sim (D_{\mathbf{N}_x \rightarrow \mathbf{M}_y, \mathbf{M}_y} \cdot D_{\mathbf{N}_x \rightarrow \mathbf{N}_x, \mathbf{N}_x})$. Contributions, which gives directionality proportional to

$\sim (D_{N_x \rightarrow N_x, N_x} \cdot D_{M_y \rightarrow N_x, M_y})$ and $\sim (D_{N_x \rightarrow M_y, M_y} \cdot D_{M_y \rightarrow M_y, N_x})$. What is demonstrated in the expression 2.6:

$$\Delta w^{unpol} \sim |a_1^{(2)} b_1^{(2)} c_1 d_1| \cos(\Delta\varphi^{pump}) \left[\alpha |a_1^{(2)}|^2 + \beta |b_1^{(2)}|^2 \right],$$

$$\alpha = D_{N_x \rightarrow M_x, M_x} D_{M_y \rightarrow M_x, N_y} - D_{N_x \rightarrow M_y, M_y} D_{M_y \rightarrow M_y, N_x},$$

$$\beta = D_{N_x \rightarrow N_x, N_x} D_{M_y \rightarrow N_x, M_y} - D_{N_x \rightarrow N_y, N_y} D_{M_y \rightarrow N_y, M_x}.$$

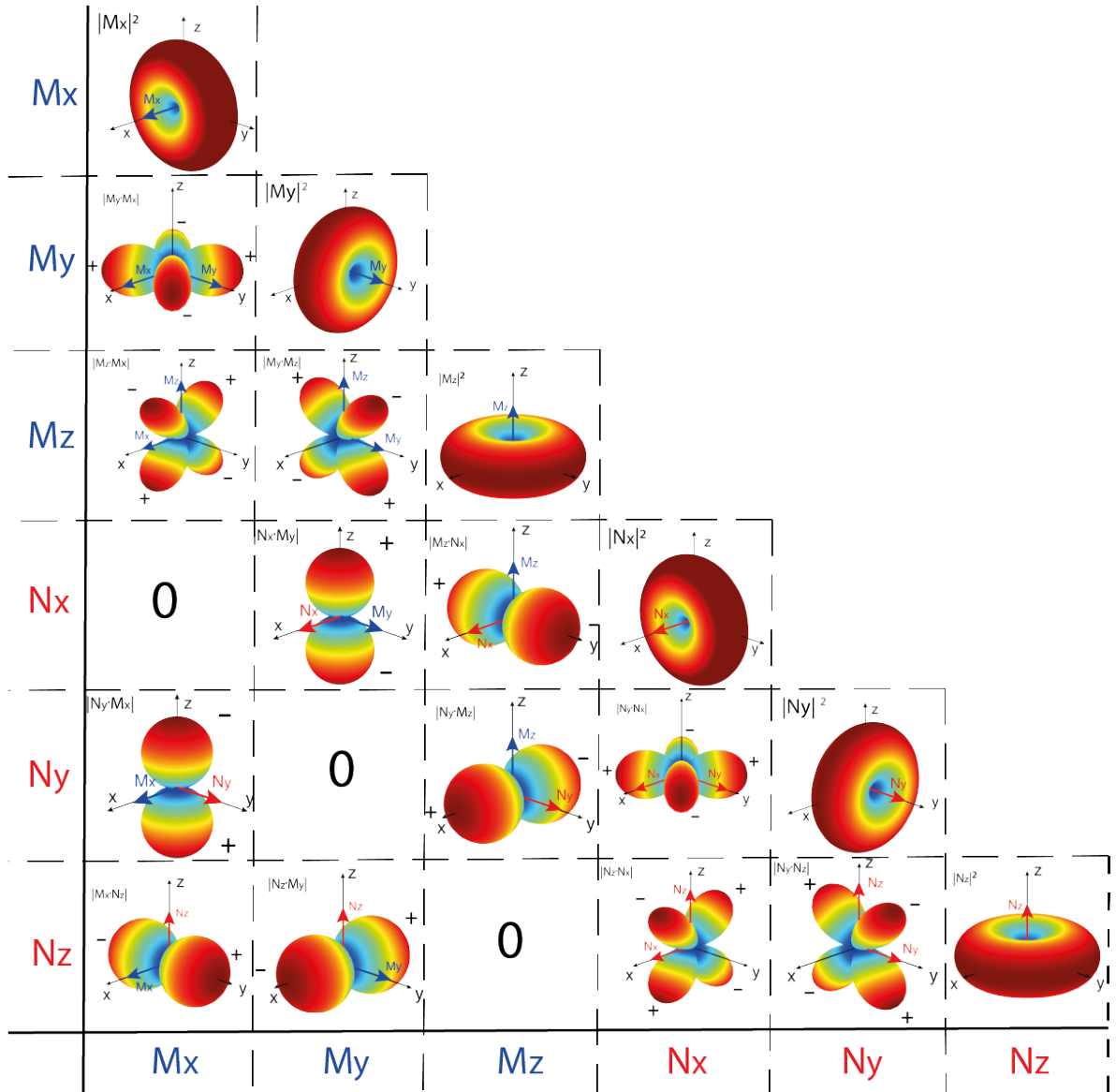


Figure A.1 — All possible variants of dipole scalar products, where the sign shows the electric field enters in phase (+) or antiphase (-)

APPENDIX B

Dimer antenna fabrication

We fabricate dimer antennas by e-beam lithography and lift-off. We spin a layer of PMMA (600K EL 4%, 4500 rpm) on a cleaned and prebaked (175°C) ITO covered glass substrate. We bake the PMMA layer at 175°C for 4 minutes. Then we spin another layer of PMMA (950K EL 2%, 2000 rpm) and bake it at 175°C for 5 minutes. We evaporate a 10 nm layer of Al. We transfer the pattern of dimer antennas by e-beam lithography. We then etch the sample in NaOH 2% for 40s and develop for 60 s in a 1:3 solution of MIBK/IPA. After RIE descum, we evaporate 3 nm of Cr and 65 nm of Au. We lift off in 50°C acetone for 10 minutes, followed by 5 minutes of ultrasonication.

Nanopositioning of BaTiO₃ nanoparticles

We spin coat a diluted solution of BaTiO₃ nanoparticles with ethanol on the dimer antennas sample. We select BaTiO₃ nanoparticles with diameters around 200 nm and employ a pick-and-place technique to position them on the center of the dimer antennas. We electrostatically pick the BaTiO₃ nanoparticle under the beam of an electron microscope using a sharp metallic tip and release it at the desired position.

Linear measurement – Dark field spectroscopy

We determine the scattering cross-section of single nanostructures (BaTiO₃ nanoparticles, dimer antennas or assembled hybrid nanostructures) in a dark-field spectroscopy setup. We focus the light from a halogen lamp on the nanostructure using a dark-field condenser (NA = 0.8-0.9). We collect the light scattered by the nanostructure with a 100x objective (Zeiss Epiplan Neofluar) and detect it using an imaging spectrometer (Andor) connected to the microscope by a 100 μ m core fiber, which acts as a pinhole. The spectrometer is equipped with a CCD camera and an InGaAs camera to determine the scattering cross-section in a broad range from 400 nm to 1500 nm. We correct the

measured signal by subtracting the background and we normalize it by the spectrum of the lamp.

Second-harmonic generation measurements

We determine the SHG spectra of single nanostructure in a home-built SHG transmission microscope. We excite the nanostructure with the laser beam from a Ti:Sapphire laser equipped with an optical parametric oscillator (Chameleon from , output wavelengths from 680 to 1600 nm). We focus the laser beam with a lens in the chosen range from 800 to 1250 nm onto the sample in steps of 5 nm and collected the transmitted laser light and the SHG using a 100x objective (NA = 0.8). We filter out the transmitted laser light and detect the SHG signal using a CMOS camera (Andor). We also control the polarization of the incident laser light with a halfwave plate mounted on a rotation stage, which allows us to measure the polar dependence of the SHG. We normalize the measured SHG spectra by the transmission of the optical components in the setup and the quantum efficiency of the camera.

Actual sizes of the samples

Table B.1 — Actual sizes of the samples and BaTiO₃ nanoparticle shifts: to x_0 along x-axis, to y_0 along y-axis and to z_0 along z-axis

| Sample | r , nm | L , nm | h , nm | w , nm | g , nm | x_0 , nm | y_0 , nm | z_0 , nm |
|---------|----------|----------|----------|----------|----------|------------|------------|------------|
| HN1(R8) | 96 | 170 | 65 | 60 | 60 | 96 | 0 | -32 |
| HN2(I8) | 95 | 170 | 65 | 60 | 60 | 24 | 49 | 0 |
| HN3(M8) | 94 | 170 | 65 | 60 | 60 | 70 | 16 | -8 |
| SP1 | 90 | - | - | - | - | 0 | 0 | 0 |
| SP2 | 90 | - | - | - | - | 0 | 0 | 0 |

Acknowledgements

The author is grateful to Petrov M.I., Frizuyk K.S., Goncharov A.S. and Solntsev A.S. for useful discussions; and to Flavia Timpu, Claude Renault, Johannes Haase, Filipp E. Komissarenko, Ivan S. Mukhin, Yuri Kivshar and Rachel Grange for performing the experiment.